Chem Soc Rev

REVIEW ARTICLE

Cite this: *Chem. Soc. Rev.*, 2021, **50**, 9741

Chemical design principles of next-generation antiviral surface coatings

Nan Wang, [a] Abdul Rahim Ferhan, [b] Bo Kyeong Yoon, [c] Joshua A. Jackman, *[c] Nam-Joon Cho *[b] and Tetsuro Majima *[a]

The ongoing coronavirus disease 2019 (COVID-19) pandemic has accelerated efforts to develop high-performance antiviral surface coatings while highlighting the need to build a strong mechanistic understanding of the chemical design principles that underpin antiviral surface coatings. Herein, we critically summarize the latest efforts to develop antiviral surface coatings that exhibit virus-inactivating functions through disrupting lipid envelopes or protein capsids. Particular attention is focused on how cutting-edge advances in material science are being applied to engineer antiviral surface coatings with tailored molecular-level properties to inhibit membrane-enveloped and non-enveloped viruses. Key topics covered include surfaces functionalized with organic and inorganic compounds and nanoparticles to inhibit viruses, and self-cleaning surfaces that incorporate photocatalysts and triplet photosensitizers. Application examples to stop COVID-19 are also introduced and demonstrate how the integration of chemical design principles and advanced material fabrication strategies are leading to next-generation surface coatings that can help thwart viral pandemics and other infectious disease threats.

Received 30th March 2021

DOI: 10.1039/d1cs00317h

rsc.li/chem-soc-rev

1. Introduction

Various emerging infectious diseases caused by viruses such as severe acute respiratory syndrome-coronavirus (SARS-CoV, also known as SARS-CoV-1), Middle East respiratory syndrome (MERS)-CoV, Ebola virus, influenza virus, norovirus, Zika virus, and dengue virus pose serious threats to human health worldwide.[1–3] In 2009–2010, a severe flu-like illness caused by a novel H1N1 strain of the influenza A virus spread rapidly

[a] *Hubei Key Laboratory of Bioinorganic Chemistry & Materia Medica, School of Chemistry and Chemical Engineering, Huazhong University of Science and Technology, Wuhan 430074, China. E-mail: t.majima@hust.edu.cn*

[b] *School of Materials Science and Engineering, Nanyang Technological University, 639798, Singapore. E-mail: njcho@ntu.edu.sg*

[c] *School of Chemical Engineering and Biomedical Institute for Convergence at SKKU (BICS), Sungkyunkwan University, Suwon 16419, Republic of Korea. E-mail: jjackman@skku.edu*

Nan Wang

Nan Wang, PhD is an Associate Professor in the School of Chemistry and Chemical Engineering, Huazhong University of Science and Technology (HUST). She earned her BS and PhD from HUST in 2005 and 2011, respectively, and completed postdoctoral studies at HUST and National Taiwan University. Her current research interests focus on the fabrication of nanomaterials such as photocatalysts, metal oxide magnetic materials, and carbon materials for the generation of reactive oxygen species in environmental applications.

Joshua A. Jackman

Joshua A. Jackman, PhD is an Assistant Professor in the School of Chemical Engineering at Sungkyunkwan University. He earned his BS degree in Chemistry from the University of Florida in 2010 and his PhD degree in Materials Science and Engineering from Nanyang Technological University in 2015, and completed postdoctoral studies at the Stanford University School of Medicine. His research focuses on lipid membrane biotechnology and the development of membrane-targeting strategies to inhibit membrane-enveloped biological nanoparticles, including viruses.

across more than 214 countries, resulting in the estimated death of over 200 000 people due to the pandemic.[4] In 2015, the Centers for Disease Control and Prevention (CDC) reported that the fatality rate from an Ebola virus outbreak in West Africa was approximately 70% among diagnosed cases.[5] Such examples highlight both the broad impact and serious health and biosecurity risks posed by viruses, especially in outbreak situations such as epidemics and pandemics.[6,7]

The ongoing coronavirus disease 2019 (COVID-19) pandemic is perhaps the greatest virus challenge faced in modern times and is caused by the severe acute respiratory syndrome-coronavirus 2 (SARS-CoV-2), which has infected over 174 million people and caused over 3.7 million deaths as of June 2021. While ongoing developments on the vaccine and antiviral therapeutic fronts offer hope for curtailing the pandemic,[8–12] there continues to be extensive attention placed on stopping community transmission and preventing virus contamination of surfaces.[13–15] These efforts have led to renewed attention on the surface contamination and decontamination of viruses in general and have also inspired the design of innovative material interfaces to curb transmission of SARS-CoV-2 and other viral threats.[16–23] To date, recent reviews covering various aspects of antiviral surface coatings[24–31] have mainly focused on conceptual descriptions and biological performance results, while there remains an outstanding need to build a deeper mechanistic understanding of how different coatings work in terms of molecular-level chemical principles.

Herein, we critically summarize the recent development of antiviral coating strategies to inactivate viruses on surfaces, including self-cleaning surfaces, along with pertinent coverage of virus stability on surfaces and the latest efforts to inactivate SARS-CoV-2 on surfaces. Particular focus is placed on distilling the chemical design principles that underpin the virus-inactivating properties of antiviral surface coatings and exploring how such mechanistic insights can guide the development of next-generation surface coatings to stop viruses and other infectious pathogens.

To create antiviral surface coatings, one may physically disrupt attaching virus particles and/or prevent the attachment process itself, and physicochemical factors such as hydrophobic interactions, electrostatic interactions, hydrogen bonding, and/or redox and coordination reactions between viruses and solid surfaces play important functional roles.[32,33] Such interactions and/or reactions are influenced by virus structure, material surface chemistry, and environmental conditions.[34–36]

Before proceeding to discuss virus interactions with surfaces, we briefly discuss the SARS-CoV-2 virus structure to give insight into potential molecular-level targets and broader implications for different types of viruses. SARS-CoV-2 belongs to the genus β-coronavirus and is a single-stranded positive-sense (ss-(+)) RNA virus with an approximately 30-kb nucleotide base length and a particle size of 60–100 nm (Fig. 1a).[37] SARS-CoV-2 encodes at least 29 proteins, four of which are structural proteins that are needed to produce a structurally complete virus particle and include the following: spike (S) glycoprotein, membrane (M) glycoprotein, envelope (E) glycoprotein, and nucleocapsid (N) phosphoprotein (Fig. 1b). S proteins assemble into homo-trimers composed of three protomers (Fig. 1c). Each S protomer comprises the receptor-binding fragment S1, the fusion fragment S2, and a single transmembrane (TM) anchor. Both S1 and S2 subunits contain a receptor binding domain (RBD), N-terminal domain, and C-terminal domain. The trimeric S protein binds to the host membrane, which is a necessary step for initiating viral fusion.[38–40] The RBD has two different conformations, with "up" and "down" representing a receptor-accessible state and a receptor-inaccessible state, respectively.[38,41] The N-terminus includes a disulphide bond (Cys15–Cys136) and an N-linked glycan at the Asn17 position (Fig. 1d). The S, M, and E proteins together with the phospholipid (PL) bilayer form the viral envelope, while the N protein interacts with genomic RNA of SARS-CoV-2 and other RNA viruses (or genomic DNA in the case of DNA viruses) to form the viral nucleocapsid.

Nam-Joon Cho

Nam-Joon Cho, PhD is the MRS-Singapore Chair Professor in the School of Materials Science and Engineering at Nanyang Technological University. He earned his BS degree in Civil Engineering from the University of California, Berkeley in 1996 and his MS degree in Materials Science and Engineering and PhD degree in Chemical Engineering from Stanford University in 2003 and 2007, respectively, and completed postdoctoral studies at the Stanford University School of Medicine. His research focuses on biomaterial strategies to develop new classes of anti-infective drugs and to create natural materials to replace plastics.

Tetsuro Majima

Tetsuro Majima, PhD is a Professor in the School of Chemistry and Chemical Engineering at Huazhong University of Science and Technology. He earned his BS, MS, and PhD degrees from Osaka University in 1975, 1977, and 1980, respectively, and completed postdoctoral studies at the University of Texas at Dallas. His current research interests focus on functional nanomaterials such as photocatalysts and PDT/PTT reagents for energy conversion, environmental, and biological applications.

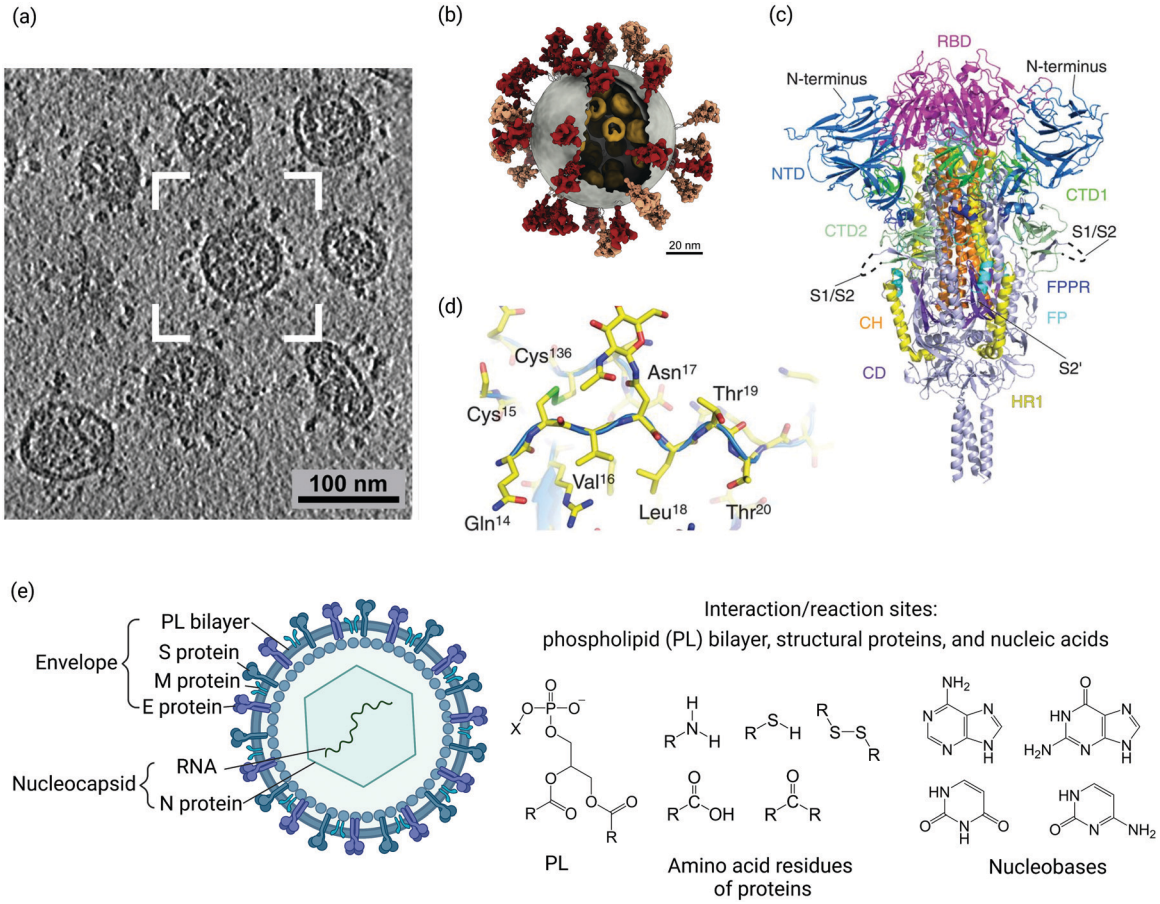

Fig. 1 Overview of virus structural components and SARS-CoV-2 example. Representative cryoelectron tomography image of SARS-CoV-2 virus particles (a).[37] Schematic illustration of an individual SARS-CoV-2 virus particle, depicting the prefusion spike (S) protein with the receptor-binding domain (RBD) domain in "down" (salmon) and "up" (red) conformations, the phospholipid (PL) bilayer envelope (grey), and ribonucleoproteins (RNPs, yellow) (b).[37] Ribbon representation of the S protein structure in the prefusion conformation, including various structural components such as the N-terminal domain (NTD), RBD, C-terminal domain 1 (CTD1), CTD2, fusion peptide (FP), fusion-peptide proximal region (FPPR), heptad repeat 1 (HR1), central helix (CH), and connector domain (CD), together with the N-terminus, S1/S2 cleavage site, and S2′ cleavage site (c).[48] Molecular model of the N-terminal segment of the S protein, where the N-terminus is located at the Gln14 residue after cleavage of the signal peptide and Cys15 forms a disulphide bond with Cys136 (d).[48] Cross-sectional representation of a SARS-CoV-2 virus particle and relevant chemical structures related to PL molecules, proteins, and nucleic acids are presented (e). While a PL bilayer is found in enveloped viruses only, proteins and nucleic acids are found in both enveloped and non-enveloped viruses.

In general, viruses that have a membrane envelope are classified as enveloped viruses, while those lacking an envelope are referred to as non-enveloped viruses (Fig. 1e). Accordingly, various antiviral surface coatings have been designed for targeting membrane-enveloped and/or non-enveloped viruses. There are three general classes of surface-coating-based mitigation strategies:[42] (1) disruption of the PL bilayer of the viral envelope; (2) damage of important proteins that are part of the envelope or capsid; and (3) degradation of nucleic acids. The chemical composition and conformation of virus components such as the PL bilayer and proteins influence the physicochemical properties and stability of viruses.[43] For example, the PL bilayer imparts negative surface charge and hydrophobic properties to virus particles. The conformation of viral proteins is also critical for necessary functions in the virus life cycle and disrupting key structural elements in viral proteins can therefore abrogate infectivity along with impairing viral nucleic acids involved in viral genome replication.[44,45] In the latter respect, the presence of reactive species such as Ag^{+}, hydroxyl radical ($^{\bullet}OH$), and singlet oxygen ($^{1}O_2$) strongly influences virus inactivation efficiency[46,47] and is an important design consideration for antiviral surface coatings.

2. Virus attachment and stability on surfaces

Viruses cannot replicate independently without a host cell, and can survive on inanimate surfaces for <5 min to >28 days, depending on surface properties, environmental conditions such as temperature, humidity, and light, and the type and amount of virus contaminant (Table 1).[42,49–56] Typically, enveloped viruses are less stable than non-enveloped viruses, because the PL bilayer has high susceptibility to physical disruption and the

Table 1 Representative examples of virus survival on surfaces in different environmental conditions

Virus	Type[a]	Diameter (nm)	Survival time [d (days), h, or min] (temperature and relative humidity (RH)) on surfaces	Ref.
SARS-CoV-2	ssRNA, E	60–140	3 d (21–23 °C, 40%) on plastic PP; 2 d (21–23 °C, 40%) on stainless steel; 4 h (21–23 °C, 40%) on Cu;	49
			3 h (22 °C, 65%) on printing and tissue paper; 2 d (22 °C, 65%) on wood and cloth; 4 d (22 °C, 65%) on glass and banknotes; 7 d (22 °C, 65%) on stainless steel and plastic; >7 d (22 °C, 65%) on the outer layer of a surgical mask;	75
			>2 d (24 °C, 20%) on stainless steel; >1 d (24 °C, 40%) on stainless steel; >1 d (24 °C, 60%) on stainless steel; >0.3 d (35 °C, 60%) on stainless steel;	76
			>28 d (20 °C, 50%) on stainless steel; >7 d (30 °C, 50%) on stainless steel; >1 d (40 °C, 50%) on stainless steel;	77
			0.5 h (65 °C, 94%) on N95 respirators	78
SARS-CoV-1	ssRNA, E	80–160	5 d (22–25 °C, 40–50%) on plastic	70
SARS-CoV-1	ssRNA, E	80–160	1 d (20 °C) on paper and cotton gown; >2 d (20 °C) on disposable gown	53
Human CoV-229E	ssRNA, E	80–160	5 d (21 °C, 30–40%) on PTFE, PVC, ceramic tiles, glass, and stainless steel; 3 d (21 °C, 30–40%) on silicon rubber; 2 h, 40 min, and 30 min (21 °C, 30–40%) on Cu–Ni alloy with 70%, 79%, and 80% Cu; 5 min (21 °C, 30–40%) on cartridge brass with 70% Cu and 30% Zn; <5 min (21 °C, 30–40%) on Cu	42
MERS-CoV	ssRNA, E	120–160	Half-life of 0.85 h (20 °C, 40%), 0.44 h (30 °C, 30%), and 0.90 (30 °C, 80%) on plastic, Half-life of 0.94 h (20 °C, 40%), 0.97 h (30 °C, 30%), and 0.64 (30 °C, 80%) on stainless steel	79
Respiratory syncytial virus	ssRNA, E	120–300	>1 d (r.t.)[b] on Al alloy (R_{rms}[c] = 0.6 ± 0.1 nm); 1 d (r.t.) on etched Al alloy (R_{rms} = 995 ± 115 nm)	64
Ebola virus	ssRNA, E	60–80	3d (27 °C, 80%) and 3 d (21 °C, 40%) on utility-grade (308) stainless steel; 3 d (27 °C, 80%) and 11 d (21 °C, 40%) on PTFE	50
Influenza A virus (H1N1)	ssRNA, E	80–120	2 d (r.t.) on wooden chopping board; 1 d (r.t.) on stainless steel and plastic; 8 h (r.t.) on cotton pillowcase	80
Influenza A virus (H1N1)	ssRNA, E	80–120	>1 d (27 °C, 50–60%) on stainless steel; 6 h (27 °C, 50–60%) on Cu	52
Parainfluenza virus	ssRNA, E	120–300	10 h (r.t.) on stainless steel and laminated plastic; 6 h (r.t.) on hospital gown, facial tissue, and laboratory coat	81
Hepatitis A virus	ssRNA, NE	20–50	9.0 d (15 °C, 30%) on chopping board; 5.4 d (15 °C, 30%), 8.4 d (15 °C, 70%), and 0.06 d (45 °C, 30%) on stainless steel	54
Hepatitis A virus	ssRNA, NE	20–50	Half-life of 169 h (5 °C, 25%), 151 d (5 °C, 50%), and 50 h (20 °C, 55%) on stainless steel	71
Mouse hepatitis virus	ssRNA, E	60–160	28 d (4 °C, 20–80%) and 5 d (20 °C, 50%) on stainless steel	51
Murine norovirus	ssRNA, NE	28–35	4.8 d (15 °C, 30%) and 6.6 d (15 °C, 70%) on chopping board	54
Murine norovirus	ssRNA, NE	28–35	14 d (22 °C) on stainless steel	82
Bovine rotavirus	dsRNA, NE	70	14 d (22 °C) on stainless steel	82
Bacteriophage MS2	ssRNA, NE	24–27	8.4 d (15 °C, 30%) and 11.4 d (15 °C, 70%) on chopping board; 19.8 d (15 °C, 30%) and 9.0 d (15 °C, 70%) on stainless steel	54

[a] ssRNA, dsRNA, E, and NE represent single-stranded RNA, double-stranded RNA, enveloped virus, and non-enveloped virus, respectively. [b] Room temperature. [c] Root-mean-square roughness.

functional conformation of envelope proteins depends on an intact bilayer environment.[57] Since enveloped viruses are surrounded by a PL bilayer and several structural proteins, they possess multiple patches of hydrophobic, hydrophilic, and positive and/or negative charges due to the presence of the PL headgroup, alkyl chains, and NH_3^+ (or NH_2) and COO^- (or COOH) groups.[32] Viruses adsorb onto a solid surface through electrostatic, hydrophobic, and/or van der Waals interactions, according to the extended Derjaguin–Landau–Verwey–Overbeek (EDLVO) theory.[58,59] For solid surfaces having hydroxyl functional groups such as glass, paper, wood, and cotton, an additional interaction, hydrogen bonding, should also be accounted, while steric effects and surface roughness should be considered for porous fomite surfaces such as paper, cardboard, and cloth.[60,61]

In general, viruses are more stable on smooth surfaces than on porous surfaces.[62,63] As the root-mean-square (RMS) roughness of an alumina alloy surface increased from 0.6 to 995 nm, the mean tissue culture infective dose ($TCID_{50}$) of respiratory syncytial virus on the surfaces decreased from 10^3 to 0 $TCID_{50}$ mL^{-1}, which occurred due to entrapment and disruption of virus on nanostructured hydrophobic surfaces.[64] SARS-CoV-1 and SARS-CoV-2 survived for 3 and 2 days on surfaces of polypropylene (PP) plastic and stainless steel, respectively, while no viable virus was observed on a Cu surface after 4 h.[49] The survival time of human coronavirus 229E on Cu alloys was

shorter than on stainless steel depending on the ratio of Cu,[42] due to the leaching of antiviral cuprous and cupric ions (Cu^{+} and Cu^{2+}, respectively) that were released from Cu.[42,65] The viral titre of influenza A virus (H1N1) at 22 °C and with humidity of 50–60% decreased from 2×10^6 to 500 and 5×10^5 plaque-forming units (PFU) mL^{-1} after 24 h on Cu and stainless steel surfaces, respectively.[52] The viral titre of influenza A virus (H1N1) decreased from 2×10^6 to 500 and 5×10^5 PFU mL^{-1} after 24 h on Cu and stainless steel surfaces, respectively.[52] The survival time of human coronavirus 229E on Cu alloys was shorter than on stainless steel depending on the ratio of Cu,[42] due to the leaching of antiviral cuprous and cupric ions (Cu^{+} and Cu^{2+}, respectively) that were released from Cu.[42,65]

Temperature and humidity both influence virus survival.[51,66,67] Viruses containing protein, RNA, or DNA are typically disrupted at >50 °C, and heat treatment at >60 °C for >1 h is sufficient to inactivate most viruses.[68] Treatment at 56 °C for 45 min completely inactivates SARS-CoV-2 with an initial viral titre of 10^6 PFU mL^{-1}.[56] As the temperature decreases from 34 °C to 14 °C at a relative humidity (RH) of 75%, the viral infectivity of the Phi6 bacteriophage (another type of virus that infects bacteria) increases exponentially by more than six orders of magnitude.[69] The influence of humidity on virus survival is neither monotonic nor consistent, while both enveloped and non-enveloped viruses with lipid envelopes and protein capsids, respectively, survive for shorter periods at moderate humidity (40–70%) than at low (≤20%) and high (≥80%) humidity.[51,54,68,70] Virus inactivation on surfaces involves desiccation-induced oxidation and Maillard reactions[71,72] as well as structural damage of lipid envelopes and protein capsids at the air–water interface in a humidity-dependent manner.[73] Temperature and humidity both influence virus survival, which also depends on the surface properties of the materials onto which a virus attaches.[51,54,68–70] SARS-CoV-1 on the dried surfaces of plastic plates survives for >5 days in a typical air-conditioned environment at 22–25 °C and with humidity of 40–50%, while there was a viral titre reduction of $10^{3.38}$-fold over 2 days at 38 °C and >95% humidity.[70] Under simulated sunlight conditions, 90% of SARS-CoV-2 virus in simulated saliva dried on grade 304 stainless steel coupons was inactivated after 6.8 and 12.8 min UVB (280–315 nm) light irradiation at 0.16 and 0.03 mW cm^{-2}, respectively, while no significant decrease in viral titre ($10^{3.0\pm0.2}$ $TCID_{50}$ mL^{-1}) occurred on the surface after 30 min drying compared with that before drying ($10^{2.8\pm0.1}$ $TCID_{50}$ mL^{-1}) in the dark.[74] Such findings are not only important for understanding virus-material interactions but can also guide material design to stop virus spreading in real-life settings.

Respiratory and enteric viruses spread directly between people and can also spread indirectly through virus-contaminated surfaces. In high-risk environments such as hospitals and public facilities, virus contaminants on high-touch surfaces such as wards, handrails, switches of lights and fans, lift buttons, and toilets spread to the hands of healthcare workers, patients, and visitors (Fig. 2).[83] Personal protective equipment (PPE) such as facial masks, protective suits, and gloves helps healthcare workers to avoid infection. However, PPE still imposes a risk of virus transmission, especially during the PPE removal step, because respiratory droplets can settle on the surface of used PPE.[84,85] Routine disinfection and cleaning of high-touch surfaces with UV light irradiation and chemicals are important and necessary for preventing virus transmission. A 9 min exposure to UV light at 254 nm and 1.94 mW m^{-2} completely inactivated a 600 μL SARS-CoV-2 solution with a concentration of 5×10^6 $TCID_{50}$ mL^{-1} in a 24-well plastic plate, which demonstrated greater efficiency than the 10-fold reduction observed under UVA light irradiation at 365 nm and 0.54 mW m^{-2}.[86] A 20 s exposure to UV light at 250–300 nm and 3.5 mW m^{-2} reduced the viral titre of 150 μL SARS-CoV-2 in a 60 mm plastic Petri dish by $>10^{3.3}$-fold.[87] Although the UV treatment of N95 masks and respirators can reduce the viral load of SARS-CoV-2 by $>10^4$-fold on N95 respirators and glass slides within 5 min,[88] viral RNA is retained.[89] Most commonly used self-cleaning materials are oxidants such as hypochlorous acid and hydrogen peroxide as well as alcohols such as ethanol and propanol.[90] Disinfection with materials such as 70% ethanol or 0.5% povidone-iodine for 15 s has also reduced the viral titre of SARS-CoV-2 in aqueous solution by $>10^{4.33}$-fold,[91] while a 5 min contact time with 10% bleach (0.6% hypochlorite), 3% H_2O_2, and a commercial QAC, Sani-Cloth AF3 germicidal disposable wipe, reduced the titre of SARS-CoV-2 on 3D-printed surgical masks by $>10^5$-fold.[92] Since disinfectant processes are labour-intensive for adequate cleaning due to chemical issues such as dewetting and volatility, self-cleaning surfaces are also being explored as a promising alternative method to prevent virus contamination by repelling virus attachment and inactivating attached virus particles.

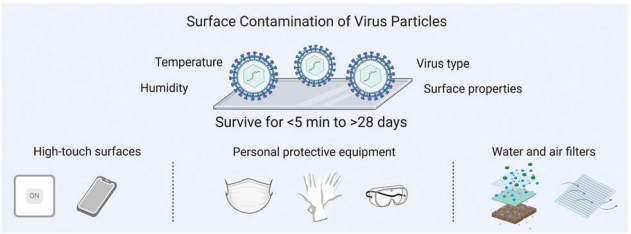

Fig. 2 Virus contamination on different types of surfaces. The extent of time during which a virus survives, *i.e.*, remains infective, depends on surface properties, environmental conditions such as temperature and humidity, and virus type.

Repelling of viruses on superhydrophobic (SHPB) surfaces is inspired by self-cleaning phenomena found in nature such as on the surfaces of lotus leaves where water droplets roll off and take away dust without leaving any trace contaminants.[93] SHPB surfaces with water contact angles (θ_{WCA}) > 150° and rolling angles (θ_{RA}) < 10° (Fig. 3a) are typically designed by decreasing surface energy and increasing surface roughness to produce an "air cushion" between the water layer and surface in the Cassie–Baxter wetting regime (Fig. 3b),[94–96] avoiding virus attachment on SHPB surfaces.[97] Polytetrafluoroethylene (PTFE) nanoparticles (NPs) with 250 nm diameter were sintered into PP textiles made from 2–8 μm fibres to produce PTFE/PP textiles with a double-roughened structure and low-surface energy functional groups of CF_2, CF_3, and CF_3CF_2 with 18, 6, and 17 mN m^{-1}, respectively,[98]

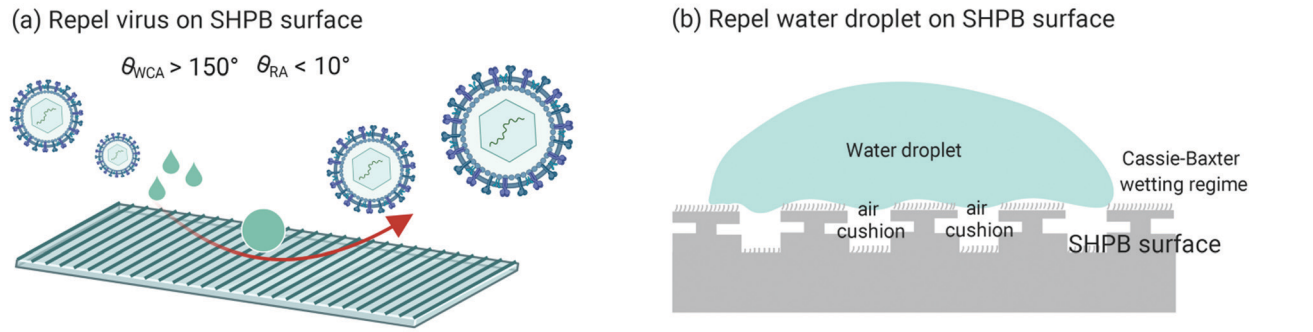

Fig. 3 Surface decontamination of viruses by repelling virus contaminants on superhydrophobic (SHPB) surfaces with water contact angle (θ_{WCA}) > 150° and rolling angle (θ_{RA}) < 10° (a). Repulsion of water droplet by air cushion between water and SHPB surface in the Cassie–Baxter wetting regime (b).

and θ_{WCA} = 160.8 ± 2.3° and θ_{RA} = 2.8 ± 1.4° indicated formation of an SHPB surface.[94] The PTFE/PP textiles prevented the attachment of adenovirus type 4 and 7a virus particles by $10^{2.1}$- and $10^{1.6}$-fold, respectively, compared to non-coated PP textiles. A nanostructured glass surface with nanopillars of 430 nm height and 100 nm diameter was prepared by a metal dewetting method and coated with trichloro(dodecyl)silane ($SiCl_3(CH_2)_{11}CH_3$, TCDDS) to produce an SHPB surface with oleophilicity (θ_{WCA} = 154° and θ_{CA} = 26° in hexadecane), and reduced viral infectivity to <10% (= inactivating activity of >90%) for influenza A virus (H3N2), as compared to <25–78% for other hydrophilic/oleophobic and hydrophobic/oleophobic surfaces with θ_{WCA} = 78–140° and θ_{CA} = 20–95° in hexadecane.[99] The difference in antiviral performance was attributed to the oleophilic surface possessing a higher affinity to interact with the fatty acid tails of PL than oleophobic surfaces, which resulted in greater disruption of the lipid membrane of enveloped viruses. It should be noted that SHPB surfaces do not inactivate virus, leading to no loss in the transferable amount of virus and no decrease in the risk of viral infection. Thus, more efforts are being directed at developing antiviral surfaces that can inactivate attached virus particles to mitigate infection risk.

3. Chemically functionalized surfaces for virus inactivation

Since viruses survive on surfaces depending on the surface properties (*cf.* Table 1), there has been extensive interest in developing functional surfaces that are coated with antiviral materials and can inactivate viruses to curb viral transmission. Antiviral material options are categorized as organic and inorganic compounds as well as metals such as quaternary ammonium compounds (QACs),[100] porphyrins,[101] TiO_2,[102] Ag,[103] and Cu[104,105] that act through different antiviral mechanisms depending on their molecular properties. Since the infectivity of enveloped and non-enveloped viruses depends on the presence of intact lipid envelopes and protein capsids, respectively, the interaction of these viral components with antiviral materials on surfaces is required for virus inactivation. The most popular organic antiviral materials are QACs that have positively charged quaternary ammonium groups and hydrophobic alkyl chains on the ammonium N atom such as alkyl or heterocyclic groups that form a lipophilic tail, which interacts with enveloped viruses through electrostatic and hydrophobic interactions that cause envelope disruption and virus particle inactivation.[106–108] Metal ions such as Ag^+ and Cu^{2+} released from metallic compounds and metal NPs, coated on surfaces, inactivate enveloped viruses through reactions with the thiol and disulfide bonds (SH and S–S, respectively) of proteins and enzymes[109–112] on lipid envelopes, and through the degradation of the helical structure of viral nucleic acids.[113,114] Practically, Cu-coated surfaces have been reported to reduce the transmission of hand-transmitted health care-associated infections by approximately 44-fold compared to control tests on stainless steel surfaces during past outbreaks caused by influenza A virus, adenovirus, and norovirus.[115] AgNPs and Ag compounds such as Ag_2O inactivate viruses due to released Ag^+.[105,116,117] Cu and cuprous compounds such as Cu_2O also inactivate viruses due to released Cu^+ and Cu^{2+},[42,118] while cupric compounds such as CuO have no or less antiviral activity.[105,116,118,119] The antiviral activity of Cu^+ is explained by the oxidative disruption properties of $^{\bullet}OH$ and superoxide ($O_2^{\bullet-}$) with oxidation potentials of $E_{ox}(^{\bullet}OH/H_2O)$ = 2.2–2.6 V and −0.28 V ($O_2/O_2^{\bullet-}$) *vs.* normal hydrogen electrode (NHE), respectively,[120,121] which are generated through the redox reaction of water and O_2 with Cu^+[52,104,105,119] as well as through the disruption of proteins upon reaction of Cu^+ with S atoms of SH and amino groups (NH_2) of cysteine amino acid residues.[118,122]

3.1. QAC-coated surfaces

QACs such as didodecyldimethylammonium bromide (DDAB) and *N*-alkylated polyethylenimines (PEIs)[100,123,124] inactivate enveloped viruses such as influenza A virus and pseudorabies virus,[108,124–126] but are less active against non-enveloped viruses such as feline calicivirus, poliovirus, and human adenovirus (Table 2).[124,127] Enveloped viruses have a hydrophobic lipid envelope membrane that is mainly composed of a negatively charged PL bilayer and several types of structural proteins (such as S, M, and E proteins for coronaviruses), while non-enveloped viruses have hydrophilic protein capsids composed of amino acids.[106,124]

For enveloped viruses, QAC-coated surfaces interact with the PL bilayer envelope through electrostatic interactions with negatively

Table 2 Virus inactivation on quaternary ammonium compound (QAC)-coated antiviral surfaces

Antiviral material	Virus[a] (N_0 [PFU mL^{-1}])[b]	Virus reduction ratio,[c] $\log_{10}(N_0/N_t)$ (exposure time)	Ref.
Didodecyldimethylammonium bromide (DDAB)-adsorbed SNP-coated glass	IAV (H1N1) (10^6)	>99%, >4.5 (6 h)	123
QAC-containing acrylic melamine-coated film	IAV (H1N1) (>10^4)	>99%, >2 (20 min)	133
$C_8H_{17}(CH_3)_2N^+(CH_2)_2OCH_3$-containing latex paint	Pseudorabies virus (1.0×10^7)	>99.9%, 4.0 (2 h)	127
	Feline calicivirus (1.0×10^7)	0% (2 h)	
$C_{16}H_{33}(CH_3)_2N^+(CH_2)_2OCH_3$-containing latex paint	Pseudorabies virus (1.0×10^7)	>99.9%, 7 (2 h)	127
	Feline calicivirus (1.0×10^7)	0% (2 h)	
$C_{16}H_{33}(CH_3)_2N^+(CH_2)_2O$ $(CH_2)_2OCH_3$-containing latex paint	Pseudorabies virus (1.0×10^7)	>99.9%, 6.9 (2 h)	127
	Feline calicivirus (1.0×10^7)	0% (2 h)	
QAC-benzophenone-based ester (BEst)-coated polyurethane (PU)	IAV (H1N1) (4.4×10^4)	99.9%, 3 (0.5 h)	135
QAC-benzophenone-based amide (BAm)-coated PU	IAV (H1N1) (4.4×10^4)	>99.9%, 4 (0.5 h)	135
N,*N*-Dodecylmethyl polyethylenimine (PEI)-coated glass	IAV (H1N1) (2×10^5)	>99.9%, >4 (0.5 h)	100
N-(15-Carboxypentadecyl) PEI-coated glass	IAV (H1N1) (2×10^5)	>99.9%, >4 (0.5 h)	100
N-(11-Carboxyundecanoyl) PEI-coated glass	IAV (H1N1) (2×10^5)	66%, 0.47 (0.5 h)	100
N-(Undecanoyl) PEI-coated glass	IAV (H1N1) (2×10^5)	6%, 0.025 (0.5 h)	100
Hyperbranched QAC polymer-coated glass	IAV (H1N1) (4×10^6)[d]	>99.9%, 5.0 (1 h)	124
	Poliovirus Sabin1 (1.6×10^7)[d]	68%, 0.5 (1 h)	
Hyperbranched QACs polymer-coated plastic	IAV (H1N1) (4×10^6)[d]	>99.9%, 3.5 (1 h)	124
	Poliovirus Sabin1 (1.6×10^7)[d]	37%, 0.2 (1 h)	
N,*N*-Dodecylmethyl PEI-coated PE	Poliovirus (2.2×10^4)	>99.9%, 4 (0.5 h)	125
	Rotavirus (5.1×10^3)	>99.9%, 3 (0.5 h)	
N,*N*-Hexylmethyl-PEI-coated glass	Poliovirus (1×10^3)	>99.9%, 3 (0.5 h)	125
N,*N*-Dodecylmethyl-PEI-coated glass	IAV (H3N2) (1.2×10^6)	>99.9%, 3.2 (0.5 h)	126
	IAV (H1N1) (6.6×10^6)	>99.9%, 4.6 (0.5 h)	
N,*N*-Dodecylmethyl PEI-coated glass	IAV (H3N2) (4.8×10^5)	>99.9%, 3.5 (5 min)	140
	IAV (H4N2) (6.1×10^6)	>99.9%, 4.5 (5 min)	
N,*N*-Dodecylmethyl PEI-coated glass	IAV (H1N1) (2.0×10^5)	>99.9%, 4.3 (5 min)	107
N,*N*-Dodecylmethyl PEI-coated PP	IAV (H1N1) (2.0×10^5)	>99.9%, 4.3 (5 min)	107
N,*N*-Dodecylmethyl PEI-coated PE	IAV (H1N1) (2.0×10^5)	>99.9%, 4.3 (5 min)	107
Permethyl PEI-coated glass	IAV (H1N1) (10^8)	92.1%, 1.10 (10 min)	108
	IAV (H3N2) (10^8)	96.5%, 1.45 (10 min)	
N-Hexyl PEI-coated glass	IAV (H1N1) (10^8)	99.8%, 2.65 (10 min)	108
	IAV (H3N2) (10^8)	99.3%, 2.15 (10 min)	
N-Dodecyl PEI-coated glass	IAV (H1N1) (10^8)	99.4%, 2.20 (10 min)	108
	IAV (H3N2) (10^8)	99.8%, 2.80 (10 min)	
N-Hexadecyl PEI-coated glass	IAV (H1N1) (10^8)	49.9%, 0.30 (10 min)	108
	IAV (H3N2) (10^8)	84.2%, 0.80 (10 min)	
N,*N*-Hexylmethyl PEI-coated glass	IAV (H1N1) (10^8)	>99.9%, 3.42 (10 min)	108
	IAV (H3N2) (10^8)	>99.9% 3.75 (10 min)	
N,*N*-Dodecylmethyl PEI-coated glass	IAV (H1N1) (10^8)	>99.9%, 3.45 (10 min)	108
	IAV (H3N2) (10^8)	>99.9%, 4.20 (10 min)	
N,*N*-Hexadecylmethyl PEI-coated glass	IAV (H1N1) (10^8)	49.9%, 0.30 (10 min)	108
	IAV (H3N2) (10^8)	88.0%, 0.92 (10 min)	
N,*N*-Hexanoylmethyl PEI-coated glass	IAV (H1N1) (10^8)	99.8%, 2.60 (10 min)	108
	IAV (H3N2) (10^8)	99.6%, 2.45 (10 min)	
N,*N*-Dodecanoylmethyl PEI-coated glass	IAV (H1N1) (10^8)	99.8%, 2.75 (10 min)	108
	IAV (H3N2) (10^8)	99.6%, 2.45 (10 min)	
PEI (5 layers)-coated polyethersulfone (PES) membranes	MS2 bacteriophage (4.0×10^8)	99%, 2 (0.5 h)	143

[a] IAV represents influenza A virus. [b] N_0 is the number of virus particles [PFU mL^{-1}] before exposure unless specified otherwise. [c] Reduction ratios are calculated from $(1 - N_t/N_0) \times 100\%$ and $\log_{10}N_0 - \log_{10}N_t$ ($= \log_{10}(N_0/N_t)$), where N_t is the number of infectious virus particles after exposure to an antiviral surface for time t. [d] N_0 is the number of virus particles with the unit of $TCID_{50}$ mL^{-1} before exposure.

charged PL headgroups and hydrophobic interactions with PL alkyl chains, which cause envelope disruption and virus inactivation (Fig. 4a).[107] The PL bilayer contains two parallel layers of PL molecules with the hydrophilic headgroups directed outwards and the hydrophobic fatty acid tails directed towards one another and forming the inner core (Fig. 4b).[128] The bilayer thickness is typically in the range of 3.6–4.0 nm for most enveloped viruses.[128] Despite this common structural feature, it is noted that the inactivation efficiency is influenced by the type of enveloped virus, which highlights the importance of additional structural elements such as the specific PL composition and envelope protein density[129–131] (Table 2). Therefore, empirical testing is warranted to identify the most effective QAC to inhibit a certain type of virus (Fig. 4c and d). By contrast, for non-enveloped viruses, the cationic quaternary ammonium groups of QACs can only interact with hydrophilic protein capsids, resulting in a lower degree of antiviral activity since the virus particles are not fully disrupted.[124,127]

For practical use in conventional paints such as anionic acrylates (latex paints), commercial QACs such as benzalkonium chloride and didecyldimethylammonium chloride need to be mixed homogeneously with paints or monomers of latex films.[127,132,133] To improve compatibility, amphiphilic QACs with alkyl and methoxyl groups, $R(CH_3)_2N^+(CH_2)_2OX$, R = C_8H_{17} or $C_{16}H_{33}$, X = CH_3 or $(CH_2)_2OCH_3$, have been used to prepare QAC-coated paints (Fig. 5a), and can reduce the viral titre by 10^4–10^7-fold for

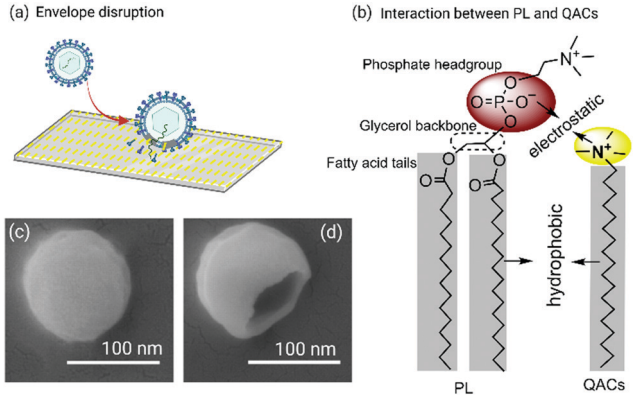

Fig. 4 Inactivation of enveloped viruses by disrupting the PL bilayer envelope through interactions with quaternary ammonium compounds (QACs) coated on the surface (a and b). Scanning electron microscopy (SEM) images of influenza virus particles after exposure to bare (c) and *N*,*N*-dodecyl, methyl-PEI-coated (d) silicon wafers.[107] The latter case is a representative QAC-coated surface that caused gross morphological disruption of virus particles.

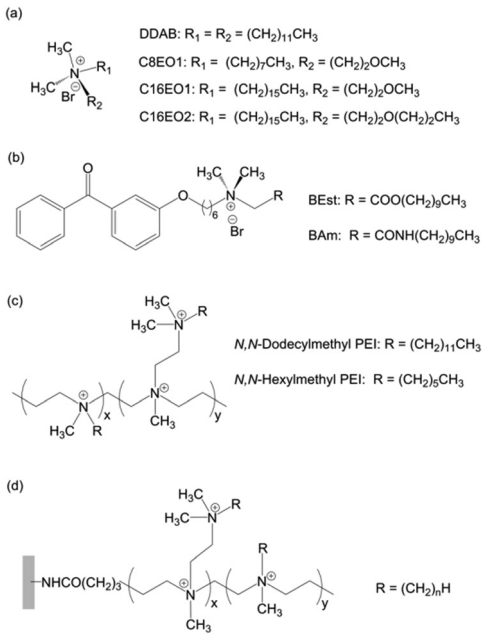

Fig. 5 Examples of several QACs and composites that are practically useful for virus inactivation on QAC-coated surfaces.

enveloped viruses such as pseudorabies virus, depending on the R substituent group of the QACs.[127] C_{16}-QACs with longer C_{16} chains have higher hydrophobicity (partition coefficient, log K_{ow} = 8.25 and 4.00 for *n*-hexadecane and *n*-octane, respectively)[134] and antiviral activity (10^7-fold reduction in viral titre) than C_8-QACs with shorter C_8 chains (10^4-fold reduction in viral titre). On the other hand, QAC-coated paints have no or less activity against non-enveloped viruses such as feline calicivirus. In terms of applications, it should be noted that there are two main challenges to incorporate QACs into water-dispersed acrylic and melamine paints: leaching from paint films found in wet environments such as bathroom faucet handles due to the water dissolution of QACs that are attached physically, *e.g.*, 0.014 mM C_{16}-QACs leached from anionic latex paint after immersion in water for 30 days;[127] and inhibiting the curing of acrylics with melamine due to electrostatic interactions between QACs and negatively charged acrylics.[133] Aromatic multicarboxylic acids such as trimesic acid were used to form ionic bonds with the quaternary ammonium groups of QACs to reduce their water solubility, while phosphoric acid (H_3PO_4) was used to neutralize the positive charge of QACs and inhibit electrostatic interactions with acrylic groups.[133] The obtained surfaces had improved antiviral activity of >99% against influenza A virus (H1N1) along with greater surface hardness (pencil hardness of H) and solvent resistance.

For glass, textile, and plastic surfaces, either encapsulating QACs in nm-/μm-sized capsules or introducing reactive functional moieties to attach QACs can also be performed by pre-coating surfaces with chemicals such as SiO_2 NPs (SNPs) and benzophenone.[123,135] For example, negatively charged SNPs with 8 nm diameter were coated with DDAB and then the DDAB-coated SNPs were adhered onto a polydopamine-functionalized glass coverslip.[123] After 30 min incubation of influenza A virus (H1N1) with a glass surface bearing attached DDAB-coated SNPs, no virus survival was observed, indicating at least 99.9% antiviral activity. By constrast, uncoated glass coverslips had no antiviral activity. In addition, catechol and aryl azide react with functional groups such as hydroxyl, amino, and carboxyl to covalently attach QACs to surfaces such as cellulose and glass,[136,137] but not to plastics such as polyethylene (PE), PP, and polystyrenes. Alternatively, a benzophenone moiety has been used to coat QACs on plastics since benzophenone is a photocrosslinker that reacts with C–H bonds through hydrogen abstraction by the triplet excited state, forming a C–C covalent bond on surfaces bearing C–H bonds.[138] QACs with benzophenone-based esters (BEst) such as 6-(4-benzoylphenoxy)-*N*-(2-(decyloxy)-2-oxoethyl)-*N*,*N*-dimethylhexan-1-aminium bromide and benzophenone-based amides (BAm) such as 6-(4-benzoylphenoxy)-*N*-(2-(decylamino)-2-oxoethyl)-*N*,*N*-dimethylhexan-1-aminium bromide have been coated on medically relevant surfaces such as cotton, PU, polyvinyl chloride (PVC), and PP, followed by UV light irradiation (Fig. 5b).[135] After 30 min exposure of influenza A virus (H1N1) to uncoated PU surfaces, there was a negligible change in viral infectivity compared to the initial viral titre of 4.4×10^4 PFU mL^{-1}, while BEst- and BAm-coated surfaces reduced the viral titre by $>10^3$- and $>10^4$-fold, respectively.

QAC-coated antiviral glass and PE materials were coated with *N*-alkylated PEIs such as *N*,*N*-dodecylmethyl PEI and *N*,*N*-hexylmethyl PEI by dipping into an *N*-alkylated PEI solution, followed by drying (Fig. 5c).[100,125,126,139,140] *N*,*N*-Dodecylmethyl PEIs with molecular weights of 2.17–217 kDa and zwitterionic *N*-(15-carboxypentadecyl)–PEI reduced the viral titre of influenza A virus (H1N1) by $>10^4$-fold within 30 min, while the viral titre reduction was only $10^{0.47}$- and $10^{0.025}$-fold for anionic *N*-(11-carboxyundecanoyl)–PEI and neutral *N*-(undecanoyl)–PEI, respectively.[100] Hyperbranched QAC polymers coated on glass and plastics reduced the infective dose of enveloped influenza A virus (H1N1) by $10^{5.0}$- and $10^{3.5}$-fold after 1 h exposure,

respectively, while there was less antiviral activity against poliovirus Sabin1 even after 6 h exposure.[124] *N*-Alkylated PEIs noncovalently coated on surfaces were stable in water but leached in organic solvents such as butanol, while *N*-alkylated PEIs covalently bonded on surfaces did not leach.[141] 4-Bromobutyryl chloride and aryl azides such as nitrophenylazide reacted with amino, hydroxyl, or carboxyl to covalently attach QACs to cotton cellulose and glass,[137,141] while benzophenone was used as a UV photocrosslinker to coat QACs on plastic surfaces such as PE and PP containing C–H groups.[142] For surfaces bearing NH_2 functional groups such as commercial NH_2-glass, covalently attached *N*-alkylated PEI coatings were prepared by *N*-acylation of surfaces with 4-bromobutyryl chloride, nucleophilic substitution of Br with PEIs, and *N*-alkylation of PEIs by haloalkyls such as $CH_3(CH_2)_6Br$ and CH_3I (Fig. 5d).[141] The obtained glass covalently bonded with branched *N*,*N*-hexylmethyl PEIs showed 99.9% antiviral activity to inhibit rotavirus and poliovirus after 0.5 h exposure.[125] Various surfaces coated by *N*-alkylated PEIs have antiviral activities against viruses such as influenza A and MS2 bacteriophage (*cf.* Table 2). The antiviral activity of glass surfaces with a covalently attached *N*-alkylated PEI coating has no correlation with various properties such as surface charge, hydrophobicity, adhesion strength, surface roughness, and polymer-chain extension length, but the degree of viral titre reduction increased from $10^{0.2}$- to $10^{3.5}$-fold upon increasing the surface density of quaternary ammonium groups from 0 to 0.12 nmol cm^{-2}.[108] Surfaces such as cotton, paper, and plastics, including PE, PP, and PVC, can be functionalized with *N*-alkylated PEIs and are expected to inhibit other enveloped viruses, albeit further testing is warranted to validate these antiviral surface coatings against current viral threats.

3.2. Ag compounds and AgNP-coated surfaces

Ag compounds such as $AgNO_3$, Ag_2O, Ag_2S, Ag^+-metal organic framework (MOF), and AgNPs have been employed as antiviral materials (Table 3). Glass surfaces coated with $AgNO_3$, Ag_2O, and Ag_2S reduced the viral titre of influenza A virus (H1N1) by $10^{6.3}$-, $10^{6.3}$-, and $10^{0.042}$-fold after 15 min exposure, while the corresponding reductions were $10^{3.3}$-, $10^{1.7}$-, and $10^{1.3}$-fold for Qβ bacteriophage after 1 h exposure, respectively.[116] These findings indicate greater antiviral activity against enveloped viruses than non-enveloped viruses. More soluble Ag_2O with a solubility limit of 0.025 g L^{-1} had greater activity than Ag_2S, which is insoluble in water, indicating that Ag^+ is responsible for virus inactivation. Ag^+-MOF prepared from Ag_2O, 1,3,5-triaza-7-phosphaadamantane, and pyromellitic reduced the titre of human adenovirus 36, a non-enveloped virus, by 10^4-fold after 30 min exposure, although the inactivation mechanism has not yet been explored.[146] The Ag^+-MOF also showed antimicrobial activity with a minimum inhibitory concentration that was >2-fold lower than that of $AgNO_3$, while the half maximal inhibitory concentration against normal human dermal fibroblasts was similar, 50.5 and 44.1 μM, for Ag^+-MOF and $AgNO_3$, respectively. Since the surface of AgNPs oxidizes to Ag_2O in water to release Ag^+,[116] AgNPs can exhibit antiviral activity for viruses such as hepatitis B virus, HIV-1, respiratory syncytial virus, and influenza A virus (Table 3),[147] with higher antiviral activity than Ag^+ by 12-fold for HIV-1.[117] It is assumed that AgNPs release Ag^0 and Ag^+ clusters with higher antiviral activity than Ag^+ although further experimental evidence is needed.[148]

It is currently understood that the antiviral activity of Ag^+ relates to the inhibition of thiol/disulphide (SH/S–S) rearrangement events that are involved in viral membrane fusion. For example, the HIV-1 E glycoprotein consists of a surface glycoprotein (gp120) and a transmembrane glycoprotein (gp41) that together form a trimer on the viral membrane surface.[144,149] HIV-1 entry requires gp120 attachment to host cell receptors, which induces a structural SH/S-S rearrangement in gp120 that is necessary for envelope fusion[144,150] (Fig. 6a and b). Because the coordination number (3.1) of amino acids containing SH for Ag^+ is larger than 0.36 and 0.28–0.4 of those containing S–S and non-sulphur moieties, respectively,[111] Ag^+ reacts preferentially with the cysteine residues (RSH and RSSR) of envelope proteins and enzymes to produce AgSR and H^+ through bond cleavage and hydrolysis, resulting in inactivation of enveloped viruses (Fig. 6c).[109–111,151]

Past studies have demonstrated that AgNPs can attach to HIV-1 virus particles and the degree of interparticle spacing (approximately 28 nm centre-to-centre distance) was similar to the expected spacing between gp120 proteins (22 nm) (Fig. 6d and e[145]), suggesting that the exposed sulphur-bearing residues of gp120 proteins are the reaction sites for AgNPs.[117,145] As a result, SH/S-S dependent membrane fusion is prevented, rendering HIV-1 inactive. Similarly, Ag^+ reacts with SH and S–S moieties in the E glycoprotein receptor of dengue virus and in the neuraminidase enzyme of influenza A virus to inactivate those enveloped viruses as well,[113,114,116,117,152] since SH/S–S exchange processes are also involved in viral infectivity processes. However, non-enveloped viruses such as coxsackie B3 virus have no such proteins or enzymes that readily react with Ag^+.[113]

From a chemical design perspective, solubility and nanoparticle size are also important.[153,154] With respect to the former point, $AgNO_3$ and Ag_2O have greater activity than Ag_2S, which is insoluble in water. With respect to the latter point, when a nanoparticle is larger than the diameter of critical protein features (approximately 15 nm), the nanoparticle will not attach to the SH/S–S region near the binding domain, resulting in lower inactivation efficiency. Accordingly, to date, AgNPs with 5–15 nm diameter have been mainly used as antiviral materials.[155] Chitosan coated with 3 wt% AgNPs with 3.5 nm diameter showed higher antiviral activity (78%) for influenza A virus (H1N1) than chitosan coated with AgNPs with 6.5 nm (60%) or with 12.9 nm (38%) diameter,[103] indicating a moderate effect of the larger surface area of smaller AgNPs. Ag^0-loaded Al_2O_3 (Ag/Al_2O_3) wafers inactivated 10^6 PFU mL^{-1} SARS-CoV-1 and baculovirus within 5 min in air, but no antiviral activity was observed in the absence of O_2,[156] indicating that the inactivation of viruses occurs by reduction of O_2 by Ag^0, generation of $^{\bullet}OH$ and $O_2^{\bullet-}$, and $^{\bullet}OH$- and $O_2^{\bullet-}$-oxidative disruption of viruses (Fig. 6f).[157] A magnetic hybrid colloid (MHC) loaded with 30 nm diameter AgNPs (Ag30/MHC) showed greater antiviral effects for ϕX174 bacteriophage and murine norovirus (10^4- and 10^6-fold reduction in viral titre, respectively)

Table 3 Virus inactivation on inorganic compound-coated antiviral surfaces

Antiviral material	Virus[a] (N_0 [PFU mL^{-1}])[b]	Virus reduction ratio,[c] $\log_{10}(N_0/N_t)$ (exposure time)	Ref.
Ag^+,Cu^{2+},Zn^{2+}-coated glass	HIV-1 (1.66×10^5)	>99.9%, 5 (20 min)	113
	HSV (1.0×10^6)	>99.9%, 5.5 (4 h)	
	DENV-2 (3.98×10^6)	97%, 2.2 (4 h)	
	IAV (H1N1) (3.63×10^5)	80%, 0.7 (4 h)	
	Coxsackie B3 virus (3.16×10^4)	37%, 0.2 (4 h)	
$AgNO_3$-coated glass	IAV (H1N1) (1.2×10^8)	>99.9%, 6.3 (0.5 h)	116
	Qβ bacteriophage (1.5×10^9)	99.9%, 3.3 (0.5 h)	
AgNP (5–25 nm)-modified graphene oxide	FCoV (4.7×10^4)[d]	92%, 1.1 (1 h)	170
	IBDV (9×10^5)[d]	96%, 1.35 (1 h)	
Mercaptoethanesulfonate-modified AgNPs (3–13 nm)	HSV-1 (2.5×10^3)	97%, 1.57 (45 min)	171
AgNPs (4–13 nm) produced by *F. oxysporum*	HSV-1 (2×10^4)	78% (2 h)	172
	HSV-2 (2×10^4)	57% (2 h)	
	HPV-3 (2×10^4)	78% (2 h)	
AgNPs (5–23 nm) produced by *C. indicum*	HSV-1 (2×10^4)	80% (2 h)	172
	HSV-2 (2×10^4)	57% (2 h)	
	HPV-3 (2×10^4)	80% (2 h)	
AgNPs (7–20 nm) produced by *Alternaria* and *Phoma* species	HSV-1 (2×10^4)	40% (2 h)	172
	HSV-2 (2×10^4)	56% (2 h)	
	HPV-3 (2×10^4)	60% (2 h)	
AgNP (7 nm)-loaded magnetic hybrid colloid (500 nm) (Ag7/MHC)	X174 bacteriophage (10^6)	99.8%, 2.7 (6 h)	158
	Murine norovirus (10^6)	90%, 1 (6 h)	
	Adenovirus serotype 2 (10^6)	49.9%, 0.3 (6 h)	
Ag15/MHC	X174 bacteriophage (10^6)	99.9%, 3 (6 h)	158
	Murine norovirus (10^6)	90%, 1 (6 h)	
	Adenovirus serotype 2 (10^6)	49.9%, 0.3 (6 h)	
Ag30/MHC	X174 bacteriophage (10^6)	>99.9%, 4 (6 h)	158
	Murine norovirus (10^6)	> 99.9%, 6 (6 h)	
	Adenovirus serotype 2 (10^6)	68.4%, 0.5 (6 h)	
AgNP (3.5 nm)-coated chitosan	IAV (H1N1) (10^3)[d]	78% (1 h)	103
AgNP (6.5 nm)-coated chitosan	IAV (H1N1) (10^3)[d]	60% (1 h)	103
AgNP (12.9 nm)-coated chitosan	IAV (H1N1) (10^3)[d]	38% (1 h)	103
PEI-(5 layers), AgNP-coated PES membranes	MS2 bacteriophage (4.0×10^8)	>99.9%, 4 (0.5 h)	143
PEI-(5 layers), AgNP-, CuNP-coated PES membranes	MS2 bacteriophage (4.0×10^8)	>99.9%, 4.5 (0.5 h)	143
Ag (0.2–12 μm)-coated glass	Qβ bacteriophage (1.5×10^9)	80%, 0.69 (0.5 h)	118
Ag/Al_2O_3 wafers	SARS-CoV-1 (10^6)	>99.9%, 6 (5 min)	156
	Baculovirus (10^6)	>99.9%, 6 (5 min)	
Ag_2O-coated glass	IAV (H1N1) (1.2×10^8)	>99.9%, 6.3 (0.5 h)	116
	Qβ bacteriophage (1.5×10^9)	98%, 1.7 (0.5 h)	
Ag_2S (3–60 μm)-coated glass	IAV (H1N1) (1.2×10^8)	9.2%, 0.042 (0.5 h)	116
	Qβ bacteriophage (1.5×10^9)	95.0%, 1.3 (1 h)	
Ag_2S (3–60 μm)-coated glass	Qβ bacteriophage (1.5×10^9)	55%, 0.26 (0.5 h)	118
AgI-coated glass	Qβ bacteriophage (1.5×10^9)	44%, 0.25 (0.5 h)	118
Ag^+-MOF	Human adenovirus 36 (10^2)[d]	>99.9%, 4 (0.5 h)	146
Cu alloy	IAV (H1N1) (2×10^6)	>99.9%, 4 (6 h)	52
Cu (42 μm)-coated Al_2O_3	MS2 bacteriophage (1.2×10^4)	>99.9%, 3.1 (2 h)	105
Cu/Al_2O_3 wafers	SARS-CoV-1 (10^6)	>99.9%, 6 (20 min)	156
	Baculovirus (10^6)	>99.9%, 6 (20 min)	156
$CuCl_2$ (500 μM)	AIV (H5N3) (10^7)	>99.9%, >5.5 (48 h)	114
$CuCl_2$ (525 μM)	FCoV (1.3×10^8)	75%, 0.6 (1 h)	119
$CuCl_2$ (250 μM)	AIV (H9N2) (10^6)	99%, 2 (1 h)	161
$CuCl_2$ (2.1 μmol)-coated glass	Qβ bacteriophage (1.5×10^9)	43%, 0.24 (0.5 h)	116
$CuCl_2$-coated glass	Qβ bacteriophage (1.5×10^9)	44%, 0.25 (0.5 h)	118
$CuCl_2$/zeolite-coated textile	AIV (H5N1) ($10^{6.7}$)	>99.9%, 5.2 (10 min)	114
	AIV (H5N3) ($10^{7.0}$)	>99.9%, 5.0 (10 min)	
CuCl (5.3 μM)	FCoV (1.3×10^8)	99%, 2.25 (1 h)	119
CuCl (2.1 μmol)-coated glass	Qβ bacteriophage (1.5×10^9)	>99.9%, 6.6 (0.5 h)	118
Cu_xO-coated N95 mask	IAV (H1N1) ($10^{5.7}$)[d]	>99.9%, 4.6 (0.5 h)	168
	AIV (H9N2) ($10^{6.2}$)[d]	>99.9%, 5.1 (0.5 h)	
Cu_xO-coated nonwoven PP fibers	Rhinovirus 2 (10^7)	99.7%, 2.5 (0.5 h)	167
	IAV (H3N2) ($10^{7.5}$)	97.8%, 1.65 (2 min)	
	Measles virus ($10^{3.67}$)	>99.9%, 3.67 (2 min)	
	RSV (10^4)	96.8%, 1.5 (2 min)	
	Parainfluenza virus 3 (10^8)	92.2%, 1.11 (2 min)	
	Adenovirus type 1 (10^5)	99.3%, 2.15 (2 min)	
	Cytomegalovirus (10^6)	>99.9%, 4.3 (2 min)	
	Vaccinia virus ($10^{7.5}$)	66.1%, 0.47 (2 min)	
Cu_2O (0.5–5 μm)-coated glass	IAV (H1N1) (1.2×10^8)	>99.9%, 3.7 (0.5 h)	116
	Qβ bacteriophage (1.5×10^9)	>99.9%, 5.8 (0.5 h)	
Cu_2O (0.5–5 μm)-coated glass	Qβ bacteriophage (1.5×10^9)	>99.9%, 5.8 (0.5 h)	118
	T4 bacteriophage (1.5×10^9)	>99.9%, 5.8 (0.5 h)	

Table 3 (*continued*)

Antiviral material	Virus[a] (N_0 [PFU mL^{-1}])[b]	Virus reduction ratio,[c] $\log_{10}(N_0/N_t)$ (exposure time)	Ref.
Cu_2O (47 μm)-coated Al_2O_3	MS2 bacteriophage (1.6×10^4)	>99.9%, 3.2 (2 h)	105
CuI-coated glass	Qβ bacteriophage (1.5×10^9)	>99.9%, 6.0 (0.5 h)	118
CuI	FCoV (1.3×10^8)	>99.9%, 7 (1 h)	119
CuI	IAV(H1N1) (10^6)	>99.9%, > 5 (1 h)	173
Cu_2S (4–95 μm)-coated glass	Qβ bacteriophage (1.5×10^9)	>99.9%, 4.6 (0.5 h)	118
CuO (0.5–40 μm)-coated glass	IAV (H1N1) (1.2×10^8)	2.3%, 0.01 (0.5 h)	116
	Qβ bacteriophage (1.5×10^9)	18.3%, 0.088 (0.5 h)	
CuO (0.5–40 μm)-coated glass	Qβ bacteriophage (1.5×10^9)	2.7%, 0.012 (0.5 h)	118
CuO (49 μm)-coated Al_2O_3	MS2 bacteriophage (1.4×10^4)	30.8%, 0.16 (2 h)	105
CuS (0.5–40 μm)-coated glass	Qβ bacteriophage (1.5×10^9)	74.3%, 0.59 (0.5 h)	118
$ZnCl_2$ (10 mM)	IAV(H1N1) ($10^{4.4}$)	90%, 2 (1 h)	169
Zn^{2+} (0.033%)-embedded PA66 fabric	IAV(H1N1) (10^4)	90%, 2 (1 h)	169

[a] IAV, AIV, HSV, DENV, HPV, RSV, and FCoV represent influenza A virus, avian influenza virus, herpes simplex virus, dengue virus, human parainfluenza virus, respiratory syncytial virus, and feline coronavirus, respectively. [b] N_0 is the number of virus particles [PFU mL^{-1}] before exposure unless specified otherwise. [c] Reduction ratios are calculated from $(1 - N_t/N_0) \times 100\%$ and $\log_{10}N_0 - \log_{10}N_t$ (= $\log_{10}(N_0/N_t)$), where N_t is the number of infectious virus particles after exposure to an antiviral surface for time t. [d] N_0 is the number of virus particles with the unit of $TCID_{50}$ mL^{-1} before exposure.

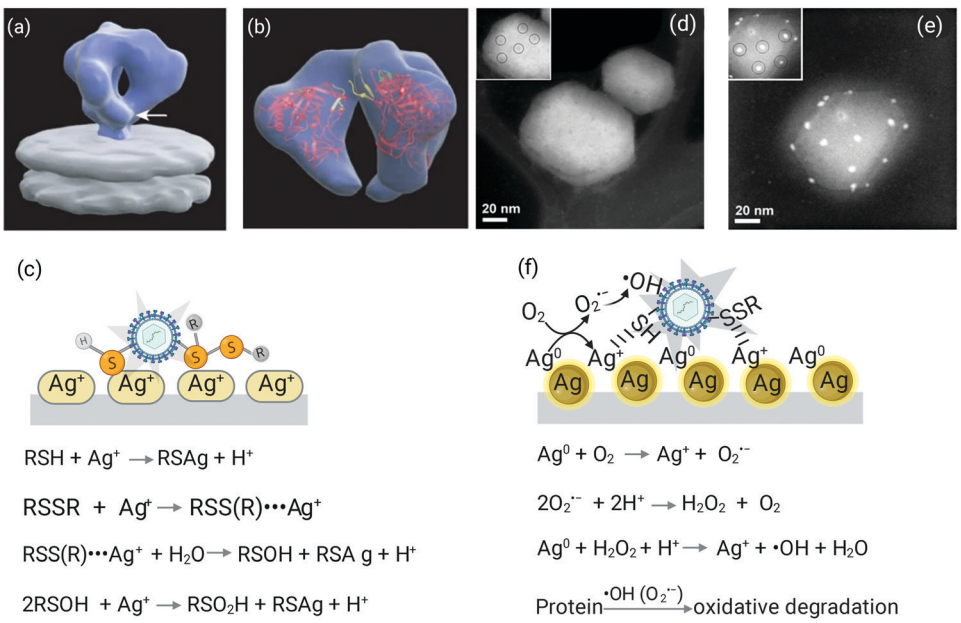

Fig. 6 Ag-mediated inactivation of viral structural proteins. 3D structure of a trimeric S protein on a native HIV-1 viral membrane (a) and gp120 core (red) derived from the complex of antibody b12 (Protein Data Bank ID, 2NY7) with V1 and V2 loops (residues 121–203, yellow) and V3 loop (residues 300–328, green) (b).[144] The white arrow (a) points to the location of gp41. Reaction of Ag^+ with cysteine residues in viral proteins (c). High angle annular dark field (HAADF) scanning transmission electron microscopy (STEM) images of HIV-1 before (d) and after (e) exposure to AgNPs.[145] Reaction of $^{\bullet}OH$ and $O_2^{\bullet-}$ generated from AgNPs with viral proteins (f).

than MHCs loaded with 7 nm diameter AgNPs (Ag7/MHC; $10^{2.7}$- and 10^3-fold reductions, respectively) and 15 nm diameter AgNPs (Ag15/MHC; 10- and 10-fold reductions, respectively), due to a higher concentration of released Ag^+ in solution from Ag30/MHC (400 mg L^{-1}) than from Ag7/MHC (57.5 mg L^{-1}) and Ag15/MHC (275 mg L^{-1}).[158] However, AgNPs/MHCs could not inactivate adenovirus serotype 2, indicating some degree of virus specificity.

3.3. CuNP, Cu alloy, and Cu compound-coated surfaces

While Ag compounds and AgNPs have high antiviral activity among metallic compounds and metal NPs, they have high costs, which limit practical applications. For this reason, Cu and Cu compound-coated surfaces have received more attention on account of the lower cost of Cu and its broader spectrum of antiviral activity against enveloped and non-enveloped viruses,[118] while Ag compounds only inactivate enveloped viruses but not non-enveloped viruses (Table 3). Cu-loaded Al_2O_3 (Cu/Al_2O_3) wafers needed 15 min longer than Ag/Al_2O_3 wafers (5 min) to completely inactivate 10^6 PFU mL^{-1} SARS-CoV-1 and baculovirus in air, and no antiviral activity was observed in the absence of O_2.[156] Cu alloy and cartridge brass surfaces with 70% Cu inactivated 10^3 PFU mL^{-1} human coronavirus 229E within 5 min by releasing Cu^+ and Cu^{2+} to induce disintegration of the viral envelope.[42]

The activity was quenched by the presence of ethylenediaminetetraacetic acid and bathocuproine disulfonate, which function as chelators of Cu^{2+} and Cu^{+}, respectively, with exposure for >2 h.

Within this scope, the inactivation of coronaviruses on Cu surfaces is considered to occur initially by released Cu^{2+}, and then by released Cu^{+} to generate $^{\bullet}OH$ and $O_2^{\bullet-}$ from the redox reaction of water and O_2.[42] Virus exposure to various reactive species such as Cu^{2+}, Cu^{+}, $^{\bullet}OH$, and $O_2^{\bullet-}$ results in the oxidation of membrane proteins and/or nucleoproteins. Although the exact inactivation mechanism is not clear, the primary interaction sites may be located on key proteins associated with viral envelopes and capsids. It has been suggested that cysteine amino acids interact with Cu(111) *via* the S atom of SH and the two O atoms of COO^{-} functional groups *in vacuo*,[159] which could explain the interaction of viral proteins and enzymes with Cu surfaces (Fig. 7a). In addition, Cu^{2+} and Cu^{+} can disrupt viruses through disrupting SH/S–S exchange of proteins *via* copper-catalysed oxidation.[160]

Antiviral activity against various viruses has been reported for Cu compounds (Table 3).[105,116,118,119] In general, cuprous compounds such as CuCl, Cu_2O, CuI, and Cu_2S have greater antiviral activity than cupric compounds such as $CuCl_2$, CuO and CuS.[114,116,118,119,161] Although the CuCl solubility limit of 0.0024 M is lower than the $CuCl_2$ solubility limit of 5.43 M in water, Cu^{+} has greater antiviral activity than Cu^{2+}. For example, the viral titre of Qβ bacteriophage decreased by $10^{6.6}$-fold after 30 min incubation on CuCl-coated glass, while the viral titre reduction was only $10^{0.24}$-fold on $CuCl_2$-coated glass. Cu^{+} from CuCl at 5.3 μM inactivated feline coronavirus with a viral titre reduction of $10^{3.3}$-fold,[119] while Cu^{2+} from $CuCl_2$ at 250 and 525 μM concentrations inactivated avian influenza virus (H9N2) and feline coronavirus with viral titre reductions of 100- and 4-fold, respectively, after 1 h exposure.[119,161]

Mechanistically, Cu^{2+} either oxidizes RSH to produce RSSR or Cu^{+}/RS^{-} complex ($Cu(SR)_2$), and H^{+}, or acts as an activator to accelerate the hydrolytic breakage of S–S bonds,[109–112] disrupting viral proteins and enzymes on lipid envelopes (Fig. 7b).[162] Cu^{2+} interacts with viral nucleic acids, such as double-stranded DNA (dsDNA) at a stability constant of 2.4×10^4 M^{-1} through bonding to nucleotides and base pairs,[113,114,163] causing degradation of the helical structure and inactivating dsDNA viruses such as herpes simplex virus.[113] Since Cu^{+} interacts with cysteine amino acids and has high affinity for the S atom of SH functional groups with 1.2 stoichiometry and a 7.9×10^9 M^{-1} stability constant, there are two possible binding configurations involving Cu^{+} and S atom binding alone or in conjunction with Cu^{+} binding to an N atom of NH_2 functional groups.[122,164] Hence, Cu^{+} can react with the SH and NH_2 groups of cysteine residues in capsid and envelope proteins (Fig. 7c). A representative example of Cu^{2+} inactivating a disulphide bond in a SARS-CoV-2 S protein is presented in Fig. 7d and demonstrates the types of protein structural elements with which Cu^{2+} can interfere.[165]

In addition, Cu^{+} induces the redox reaction of water and O_2 to generate $^{\bullet}OH$ and $O_2^{\bullet-}$ for inactivating viruses through oxidative disruption.[119] Cu^{+} initially reduces O_2 to produce Cu^{2+} and $O_2^{\bullet-}$, followed by the formation of H_2O_2 from the redox reaction of $O_2^{\bullet-}$ with water and the generation of $^{\bullet}OH$ from the reaction between Cu^{+} and H_2O_2. Since $^{\bullet}OH$ reacts with cysteine, tryptophan, and tyrosine residues at rates of $(1.3–3.5) \times 10^{10}$ M^{-1} s^{-1} that are faster than the rates of 1.7×10^7–8.5×10^9 M^{-1} s^{-1} for

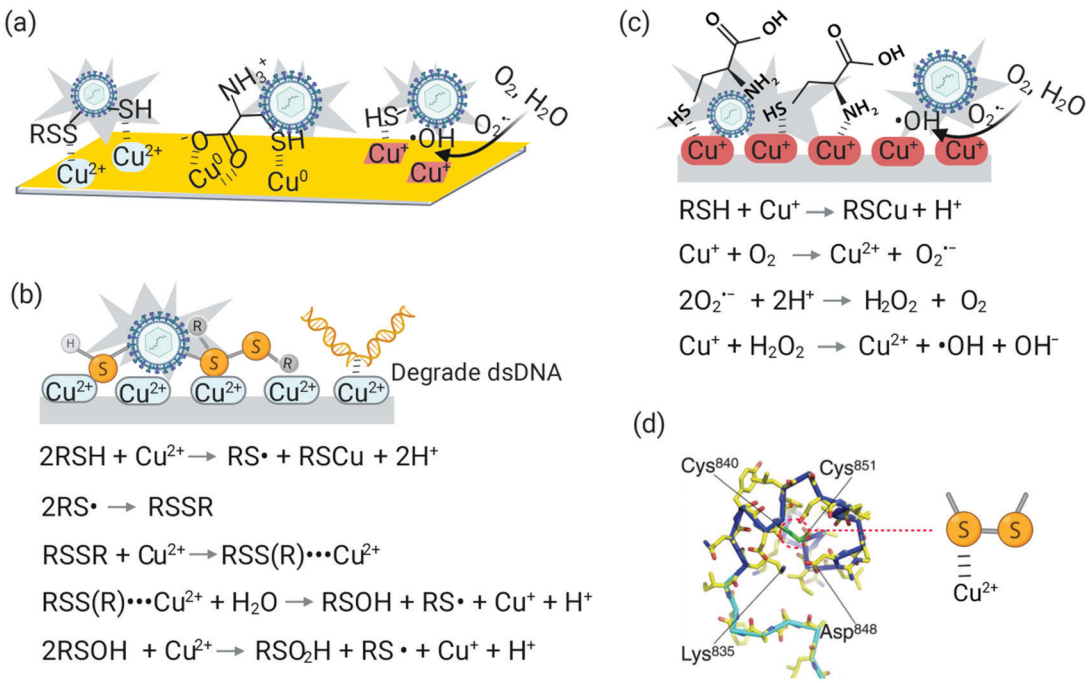

Fig. 7 Virus inactivation on surfaces coated with a Cu alloy or NPs (a), $CuCl_2$ (b), or cuprous compounds such as CuCl, Cu_2O, and CuI (c). Illustrative example of Cu^{2+} interaction with a disulphide bond in the S protein[48] of SARS-CoV-2 (d).

other amino acids,[166] the initial oxidation is suggested to occur on those particular amino acids found within viral proteins and enzymes.

A Cu_xO-coated filter inactivated influenza A virus (H1N1) with a viral titre reduction of 59-fold after 40 min filtration,[167] and a Cu_xO-coated face mask inactivated influenza A virus (H1N1) and avian influenza virus (H9N2) by 10^3-fold after 30 min filtration,[168] although the oxidation states of Cu were not reported. Cuprous compounds such as Cu_2O and Cu_2S reduced the viral titre by $10^{3.7}$-, $10^{3.2}$-, and $10^{5.8}$–10^6-fold for influenza A virus (H1N1),[116] MS2 bacteriophage,[105] and Qβ bacteriophage,[118] at 0.5, 2, and 0.5 h, respectively, while cupric compounds such as CuO and CuS had no or less activity with viral titre reductions around only $10^{0.01}$–$10^{0.59}$-fold (Table 3).[105,116,118,119] The lower activity of CuO and CuS is due to the lower activity of Cu^{2+} compared to that of Cu^+.[119] Cu_2O (2.1 μmol)-coated glass released Cu^{2+} and Cu^+ at 21.6 and 7.19 μM concentrations, respectively, and yielded negligible inactivation of Qβ bacteriophage with a viral titre reduction of only $10^{0.2}$-fold.[118] When filter paper with 105 μm thickness and 30 nm pore size was placed on Cu_2O- or Cu_2O-modified by 1*H*-benzotriazole-coated glass, the viral titre reduction of Qβ bacteriophage decreased from around $10^{5.8}$- to $10^{1.2}$- and $10^{0.6}$-fold, respectively,[118] which supports that the direct interaction between cuprous compounds and Qβ bacteriophage is important for virus inactivation. An 8 h exposure of bovine serum albumin protein led to strong adsorption on Cu_2O-coated, but not CuO-coated, surfaces and 1 h incubation of alkaline phosphatase enzyme in Cu_2O suspensions led to a 70% decrease in the enzymatic activity *via* denaturation, including 30% adsorption-related loss, while there was no change in enzymatic activity upon incubation in CuO suspensions.[118] The interaction of Cu_2O with viral capsid proteins through the S atom of SH and N atom of NH_2 groups in cysteine residues[122] was suggested to cause the disruption of viral proteins and enzymes by Cu^+ released from Cu_2O (*cf.* Fig. 7c).[116] CuI at 1000 mg L^{-1} (5.26 mM) in water released Cu^{2+} and Cu^+ at 426.4 and 3.6 μM concentrations, respectively, which resulted in the inactivation of feline calicivirus with a viral titre reduction of $10^{6.2}$-fold after 1 h exposure.[119] Comparably, the viral titre reduction of feline calicivirus was 4- and $10^{3.3}$-fold upon treatment with $CuCl_2$ and CuCl at 525 and 5.3 μM, respectively. Together, these data suggest that the contact of feline calicivirus with CuI surfaces is better for virus inactivation. Since the Trp383 and Met651 residues in the capsid protein of feline calicivirus were oxidized to tryptophan-OH and methionine sulfoxide, respectively, the inactivation corresponds to oxidative disruption by Cu^+ in spite of its two-orders of magnitude lower concentration than that of Cu^{2+}.[119]

In addition to Ag and Cu compounds, 10 mM $ZnCl_2$ inactivated influenza A virus (H1N1), resulting in a viral titre reduction of 99% after 1 h exposure.[169] It was found that $ZnCl_2$ reduced 30% of haemagglutinin proteins, while there was no effect on neuraminidase enzymes or viral RNA. These findings implied that Zn^{2+} can inactivate influenza A virus (H1N1) through the destabilization of surface proteins rather than internal proteins or nucleic acids. Zn^{2+} (0.033%)-embedded polyamide 6.6 (PA6.6) fabric reduced the viral titre of influenza A virus (H1N1) by a 10^2-fold higher extent than a PA66 control fabric. Interestingly, a glass surface coated with $AgNO_3$, $Cu(NO_3)_2$, and $Zn(NO_3)_2$ resulted in viral titre reductions of 99.9% after 20 min exposure of HIV-1, while the corresponding reduction levels were 99.9, 97, 77, and 37% for herpes simplex virus type 1, dengue virus type 2, influenza A virus (H1N1), and coxsackie B3 virus, respectively,[113] which indicated different sensitivities of viruses to Ag^+, Cu^{2+}, and Zn^{2+}.

As noted above, there are many types of chemically functionalized surfaces for virus inactivation. Surfaces coated by QACs such as DDAB and *N*-alkylated PEIs exhibit antiviral activity against enveloped viruses, and QACs covalently bonded on surfaces have non-leaching properties (Table 3). The antiviral activity of QACs decreases with increasing the operating time due to the accumulation of inactivated viruses on surfaces. On the other hand, the antiviral activity exhibited by AgNPs, CuNPs, and Ag, Cu, and Zn compounds is mainly due to released metal ions on the surface, which occurs through different mechanisms. AgNPs have greater antiviral activity against enveloped viruses than CuNPs, but the high cost of Ag limits practical application along with ineffectiveness against non-enveloped viruses. On the other hand, Cu-coated surfaces have received more attention due to the lower cost of Cu and since Cu and cuprous compounds such as Cu_2O, CuI, and CuCl can exhibit antiviral activity against both enveloped and non-enveloped viruses.

4. Light-induced surfaces for virus inactivation

While photocatalysts and triplet photosensitizers such as TiO_2 and porphyrins have no antiviral activity in the dark, they can inactivate viruses under light irradiation through photocatalysis and triplet photosensitized reactions, respectively. The photocatalytic disruption of viruses is generally considered to proceed through oxidation by the photogenerated holes of photocatalysts, and oxidation by oxidative reactive oxygen species (ROS) such as $^{\bullet}OH$ and $O_2^{\bullet-}$ that are generated through the redox reaction of water and O_2 with photogenerated holes and electrons.[174] Triplet photosensitized disruption of viruses proceeds through oxidation by $^1O_2$ that is generated by triplet–triplet energy transfer from triplet photosensitizers to O_2.[175] Such ROS react initially with the amino acids of proteins found in lipid envelope and capsid structures to inactivate viruses depending on the virus type. Light-induced virus inactivation can be divided into two classes depending on whether UV or visible light irradiation is required to render the surface functional. The corresponding mechanisms are discussed below.

4.1. UV light-driven TiO_2 photocatalyst-coated surfaces

Photocatalytic disruption of viruses[101,200,201] is considered to proceed through oxidation by photogenerated holes on photocatalyst surfaces, and by ROS such as $^{\bullet}OH$ and $O_2^{\bullet-}$ generated from the redox reaction of water and O_2 with photogenerated holes and electrons under light irradiation (Fig. 8a and b).[202,203] Oxidative disruption of lipid envelopes and protein capsids by

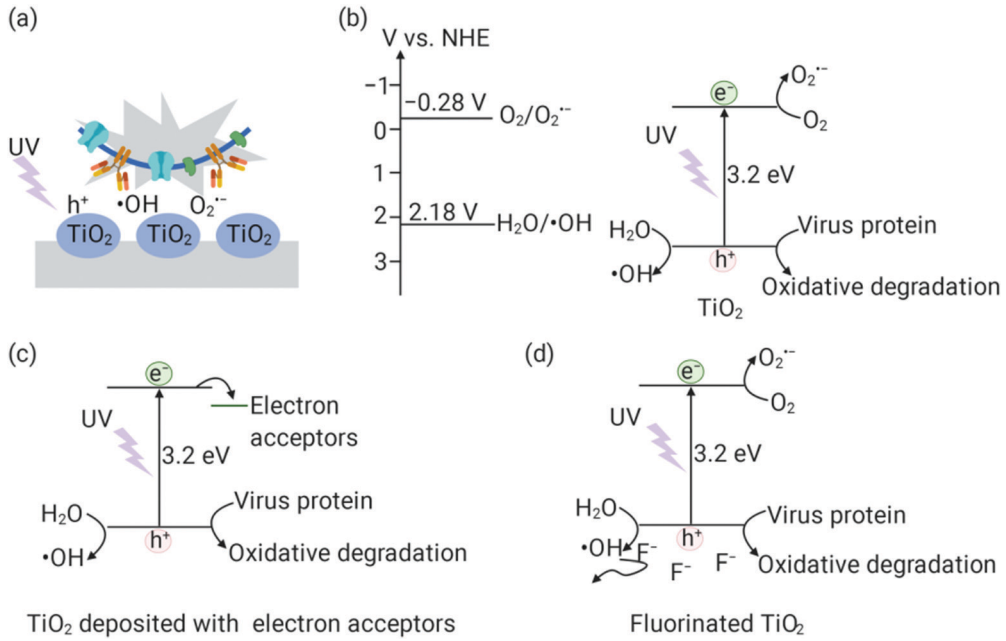

Fig. 8 Virus inactivation on surfaces coated with TiO_2 as a photocatalyst under UV light irradiation (a). Generation of $^{\bullet}OH$ and $O_2^{\bullet-}$ from the band-gap excitation of TiO_2 (b) and enhancement of $^{\bullet}OH$-oxidation by deposition of electron acceptors on TiO_2 (c) or fluorination of TiO_2 (d).

photogenerated holes occurs on the photocatalyst surface through hole transfer, and even in air by ROS that diffuse from the surface.[201,204] The degree of virus-inactivating activity increases with a greater amount of tyrosine residues in viral proteins, since tyrosine has the highest $E_{HOMO} = -8.81$ eV[201] and lowest $E_{ox} = 0.97$ V *vs.* NHE at pH = 7[205] among amino acids found in envelope and capsid proteins. Coating TiO_2 on membranes, filters, and films has also been shown to inactivate bacteriophages such as MS2 and Qβ and mammalian viruses such as respiratory syndrome virus and influenza virus that are attached to surfaces in an air environment under UV light irradiation (Table 4). For example, coating TiO_2 on a cell culture plate reduced the viral titre of avian influenza virus (H9N2) from 10^4 to $10^{2.72}$ PFU mL^{-1} under UV light irradiation at 0.5 mW cm^{-2} for 1.5 h.[176] A titanium apatite photocatalyst-coated filter inactivated SARS-CoV-1 with an initial infectivity of $10^{7.5}$ PFU mL^{-1} under UV light irradiation at 1 mW cm^{-2} for 6 h.[177] A TiO_2-coated aluminium filter inactivated influenza A virus (H1N1) by reducing aerosol-associated infectivity of $(1.2–2.6) \times 10^6$ PFU mL^{-1} to an undetectable level of infectivity (<300 PFU mL^{-1}) under 375 nm light irradiation at 10 mW cm^{-2} for 7 min.[178]

A high concentration of photogenerated holes and ROS as well as close contact between viruses and TiO_2 can increase the level of photocatalytic inactivating activity. Anatase TiO_2 doped with electron acceptors such as metals and semiconductors as well as fluorinated TiO_2 inactivated viruses with higher activity than TiO_2, due to enhancing photogenerated charge separation and oxidation of H_2O and OH^- by photogenerated holes (see Fig. 8c and d).[206–209] For example, TiO_2 surfaces with 2 nm diameter AgNP deposits inactivated MS2 bacteriophage at a 5.8-fold quicker rate than TiO_2 alone under UV light irradiation at 2.5 mW cm^{-2} for 2 min (Table 4).[180] The degree of photocatalytic virus-inactivating activity decreased by $10^{4.2}$–$10^{4.7}$-fold in the presence of methanol and *t*-butanol, which acted as scavengers of photogenerated holes and $^{\bullet}OH$, suggesting that both species are involved.[180] A mixture of anatase and rutile TiO_2 with a ratio of 7 : 3 reduced the viral titre of MS2 bacteriophage by $10^{1.9}$-fold after 1.5 min exposure, which was higher than the results achieved using pure anatase and rutile TiO_2 that yielded $10^{1.0}$ and $10^{0.75}$-fold reductions, respectively, suggesting enhanced charge separation at the interface between anatase and rutile TiO_2.[184] Fluorination of TiO_2 surfaces by adsorption of F^- inactivated MS2 bacteriophage by a two-orders of magnitude greater degree than TiO_2 under UV light irradiation at 10 μW cm^{-2} for 1 h.[182] TiO_2 (P25) with SNP deposits reduced the viral titre of MS2 bacteriophage by $10^{5.5}$-fold after 1.5 min exposure, which was four-orders of magnitude greater than the $10^{1.5}$-fold reduction level achieved using TiO_2 under UV-A light (315–400 nm) irradiation at 2.5 mW cm^{-2}.[183] The adsorption of MS2 bacteriophage increased by 37-fold for TiO_2 surfaces with SNP deposits,[183] suggesting that the interface between negatively charged SNPs and positively charged TiO_2 enhances adsorption due to charge heterogeneity of MS2 bacteriophages[210] and that direct oxidation of adsorbed MS2 bacteriophage by photogenerated holes is the initial process during photocatalysis.

4.2. Visible light-driven photocatalyst-coated surfaces

Due to its wide band gap of ≥ 3.0 eV,[211] TiO_2 exhibits photocatalytic virus-inactivating activity under UV light irradiation. Visible light (400–700 nm)-driven TiO_2 doped with metal ions,[186] metal oxides,[185] and non-metal anions,[188] as well as other visible-light-responsive semiconductors such as g-C_3N_4,[187,189] WO_3,[190–192] $BiWO_4$,[187] and Ag/AgCl[187] inactivated viruses under visible light

Table 4 Virus inactivation on photocatalyst- and triplet photosensitizer-coated surfaces

Photocatalyst- or triplet photosensitizer-coated surface	Virus[a] (N_0 [PFU mL^{-1}])[b]	Light source, wavelength, power	Virus reduction ratio,[c] $\log_{10}(N_0/N_t)$ (exposure time)	Ref.
TiO_2-coated glass	IAV (H1N1) (10^8)	Black light lamp, 300–425 nm, 0.1 mW cm^{-2}	>99.9%, 4 (8 h)	102
TiO_2-coated cell culture plate	AIV (H9N2) (10^4)	Black light lamp, 365 nm, 0.5 mW cm^{-2}	99.8%, 2.72 (1.5 h)	176
Titanium apatite-coated filter	SARS-CoV-1 ($10^{7.5}$)	UV lamp, 365 nm, 1 mW cm^{-2}	>99.9%, 4 (6 h)	177
TiO_2-coated aluminium filter	IAV (H1N1) ($(1.2–2.6) \times 10^6$)	UV-LED lamp, 375 nm, 10 mW cm^{-2}	>99.9%, 3.9 (7 min)	178
TiO_2 (P25)-coated ceramic membrane	MS2 bacteriophage (10^5) ΦX174 bacteriophage (10^5) PR772 bacteriophage (10^5)	UV tubes, 253 nm, 1.7 mW cm^{-2}	99.9%, 3 (0.25 h) 99.9%, 3 (5.8 h) 99.9%, 3 (>20 h)	179
TiO_2 (P25)-coated glass 5.95%Ag/TiO_2 (P25)-coated glass Anatase TiO_2-coated glass 3.94% Ag/anatase TiO_2-coated glass	MS2 bacteriophage (7×10^9)	UV-A lamp, 315–400 nm, 2.5 mW cm^{-2}	>99.9%, 4.0 (5.1 min) >99.9%, 5.4 (1.5 min) >99.9%, 4.0 (16.7 min) 99.8%, 2.8 (1.5 min)	180
Cu/TiO_2 (1 : 5.5) non-woven fabric	HNV ($10^{6.7}$ genomic copies m^{-3})	UV-A LED, 365 nm, 5000 mW cm^{-2}	>99.9%, 3.8 (1 h)	181
TiO_2 (P25)-coated glass	MS2 bacteriophage (10^{10}) Feline calcivirus (10^8) Murine norovirus ($10^{8.9}$)	Fluorescent lamp, 365 nm, 10 μW cm^{-2}	85.9%, 0.85 (1 h) 80.9%, 0.72 (1 h) 70.5%, 0.53 (1 h)	182
Fluorinated TiO_2 (P25)-coated glass	MS2 bacteriophage (10^{10}) Feline calcivirus (10^8) Murine norovirus ($10^{8.9}$)	Fluorescent lamp, 365 nm, 10 μW cm^{-2}	99.8%, 2.6 (1 h) 99%, 2.0 (1 h) 99.8%, 2.6 (1 h)	182
TiO_2 (P25)-coated glass 5% SiO_2 (SNPs)/TiO_2 (P25)-coated glass	MS2 bacteriophage (3×10^7)	UV-A lamp, 350 nm, 2.5 mW cm^{-2}	98.4%, 1.8 (1.5 min) >99.9%, 5.5 (1.5 min)	183
Anatase TiO_2-coated glass Rutile TiO_2-coated glass Mixed-phase TiO_2- coated glass	MS2 bacteriophage (10^9)	Black light lamp, 300–425 nm, 2.2 mW cm^{-2}	90%, 1.0 (1.5 min) 82.2%, 0.75 (1.5 min) 98.7%, 1.9 (1.5 min)	184
0.25% Cu_xO(Cu^+/Cu^{2+} = 0.13)/TiO_2-coated glass 0.25% Cu^{2+}/TiO_2-coated glass	Qβ bacteriophage (1.2×10^{11})	White light bulbs, >400 nm, 800 lux (0.12 mW cm^{-2})	>99.9%, 7.5 (40 min) 99.2%, 2.1 (1 h)	185
Cu^{2+}/TiO_2-coated nanofiber (Cu : Ti = 1 : 7)	f2 bacteriophage (10^5)	Xenon lamp, >400 nm, 100 mW cm^{-2}	>99.9%, 5 (1 h)	186
$TiO_{2-x}N_x$-coated glass	MS2 bacteriophage (10^8)	Xenon-arc lamp, >400 nm, 150 mW cm^{-2}	90%, 1 (5 h)	187
PdO/$TiO_{2-x}N_x$ nanofiber (Pd : N : Ti = 0.03 : 0.1 : 1)	Coliphage MS2 (3×10^8)	Xenon-arc lamp, >400 nm, 100 mW^{-2}	95.0%, 1.3 (1 h)	188
Bi_2WO_6-coated glass Ag/AgCl-coated glass g-C_3N_4-coated glass	MS2 bacteriophage (10^8)	Xenon-arc lamp, >400 nm, 150 mW cm^{-2}	>99.9%, 4 (5 h) >99.9%, 8 (5 h) >99.9%, 7.5 (5 h)	187
g-C_3N_4 Ag_3PO_4 (200 nm) Ag_3PO_4/g-C_3N_4	f2 bacteriophage (3×10^6)	Xenon lamp, >400 nm, 30 mW cm^{-2}	>99.9%, 3.5 (80 min) >99.9%, 4.5 (80 min) >99.9%, 6 (80 min)	189
Graphene/WO_3-coated glass	MS2 bacteriophage (2×10^6)	Mercury lamp, >400 nm, 110 mW cm^{-2}	>99.9%, 5 (3 h)	190
Pt/WO_3-coated PE terephthalate film	AIV (H1N1) ($10^{4.7}$)[d] Qβ bacteriophage (10^9) AIV (H1N1) ($10^{4.8}$)[d] Goose parvovirus ($10^{4.6}$)[d]	LED, 410–750 nm, 150 lux (22 μW cm^{-2})[e] LED, 410–750 nm, 1000 lux (0.15 mW cm^{-2})[e]	>99.9%, 3.2 (2 h) >99.9%, 4 (2 h) >99.9%, 3.3 (2 h) 99.7%, 2.5 (2 h)	191
Pt/WO_3-coated glass	AIV (H1N1) (10^7)[d]	Fluorescent lamp, >410 nm, 1000 lux (0.15 mW cm^{-2})[f]	>99.9%, 5.5 (2 h)	192
DIMPy-BODIPY	DENV-1 (6.5×10^6)[e] VSV (10^7) HAdV-5 (6.5×10^5)	Xenophot bulb, 400–700 nm, 65 mW cm^{-2}	>99.9%, 4 (0.5 h) >99.9%, 5 (0.5 h) 99%, 2 (0.5 h)	193
DIMPy-BODIPY-coated PAN nanofibers	VSV (10^6)	Xenophot bulb, 400–700 nm, 65 mW cm^{-2}	>99.9%, 4 (1 h)	194
TMPyP	MS2 bacteriophage ($10^{4.4}$) Hepatitis A Virus ($10^{4.4}$)	UV lamp, 365 nm, 2.2 mW cm^{-2}	>99.9%, 4.1 (10 min) >99.9%, 3.7 (10 min)	195
TMPyP-coated PAN nanofibers	VSV (5×10^8) HAdV-5 (4.5×10^7)	Xenophot bulb, 400–700 nm, 65 mW cm^{-2}	>99.9%, 7 (0.5 h) >99.9%, 5 (0.5 h)	101
Benzophenone-polyphenol-coated PVA-*co*-PE nanofibrous membranes	T7 bacteriophage (10^5)	D65 Daylight lamp, 300–800 nm, 6.5 mW cm^{-2}	>99.9%, 5 (5 min)	196
Buckminster fullerene (C_{60})	Semliki forest virus (10^9)[d] VSV (10^9)[d]	Mercury short-arc lamp, 495 nm, 2×10^5 lux (29.4 mW cm^{-2})	>99.9%, 7 (6 h) >99.9%, 7 (6 h)	197
C_{60}/amine-modified-SiO_2-coated stainless steel mesh	MS2 bacteriophage (10^5)	Blue LED, 470 nm, 18.8 mW cm^{-2}	97.8%, 1.6 (1.5 h)	198

[a] IAV, AIV, DENV, VSV, HAdV-5 and HNV represent influenza A virus, avian influenza virus, dengue virus, vesicular stomatitis virus, human adenovirus-5, and human norovirus respectively. [b] N_0 is the number of virus particles [PFU mL^{-1}] before exposure unless specified otherwise. [c] Reduction ratios are calculated from $(1 - N_t/N_0) \times 100\%$ and $\log_{10}N_0 - \log_{10}N_t$ ($= \log_{10}(N_0/N_t)$), where N_t is the number of infectious virus particles after exposure to an antiviral surface for time t. [d] N_0 is the number of virus particles with the unit of $TCID_{50}$ mL^{-1} before exposure. [e] N_0 is the number of virus particles with the unit of focus-forming unit (FFU mL^{-1}) before exposure. [f] The light intensity with the unit of lux is converted to that with the unit of μW cm^{-2} by 1 lux = 0.146 μW cm^{-2}.[199]

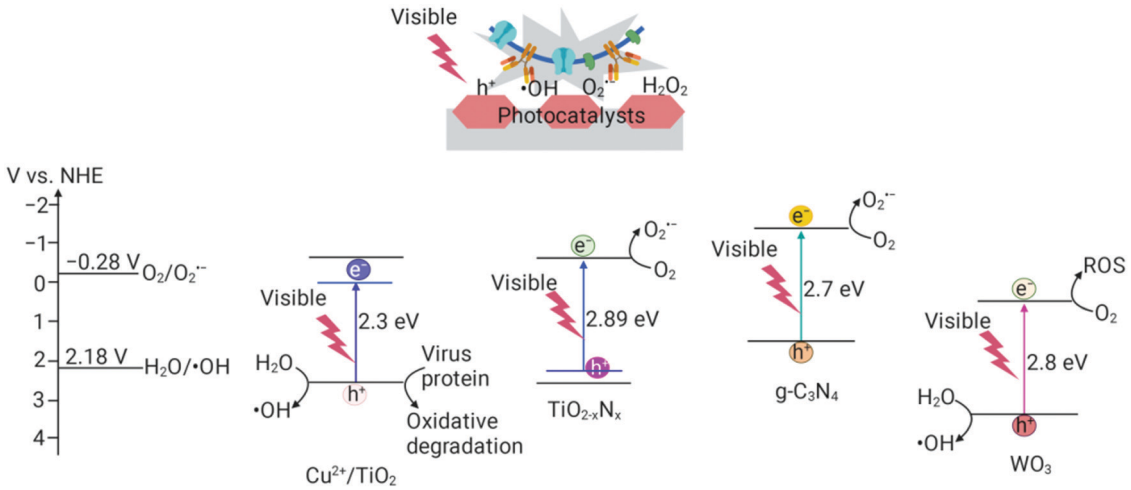

Fig. 9 Virus inactivation on surfaces coated with visible light-driven photocatalysts such as Cu^{2+}/TiO_2, $TiO_{2-x}N_x$, g-C_3N_4, and WO_3 under visible light irradiation.

irradiation using daylight sources such as a D65 standard daylight lamp, indoor lamps such as white fluorescent/incandescent lamps, white light emitting diodes (LEDs), and a Xenon lamp with filters for sunlight or visible light (Table 4 and Fig. 9). Although visible-light-responsive TiO_2 photocatalysts are known to inactivate viruses, the effects of many related aspects such as the inhibitory mechanisms, reactive species involved, reaction sites, temperature effects, and so forth are still being unravelled. Substituting Ti^{4+} and O^{2-} with metal ions such as Cu^{2+} and anions such as N and S in the crystal lattice of TiO_2 generates impurity energy levels below the conduction band (CB) and above the valence band (VB) of TiO_2, respectively, causing visible light absorption and changing the redox properties.[212–215] Substituting Ti^{4+} with metal ions such as Cu^{2+} in the crystal lattice of TiO_2 generates impurity energy levels below the CB of TiO_2, causing visible light absorption and inactivating viruses. TiO_2 nanofibers doped with Cu^{2+} (Cu^{2+}/TiO_2) were prepared by *in situ* incorporation *via* electrospinning of a precursor solution comprising tetrabutyl titanate, cupric nitrate, acetic acid, PVP, and anhydrous alcohol, and post-treatment of the as-spun nanofibers in a furnace to facilitate thermal decomposition of PVP at 450 °C in air, to have a diameter of 100 nm, band gap of 2.30 eV, and Cu^{2+} doped into the crystal lattice of anatase TiO_2 at the atomic ratio of Cu : Ti = 1 : 7, which caused inactivation of f2 bacteriophage with a viral titre reduction of 10^5-fold under visible light irradiation at 100 mW cm^{-2} for 4 h.[186] TiO_2 doped with Cu_xO (0.25% Cu_xO/TiO_2, Cu^+/Cu^{2+} = 0.13) inactivated Qβ bacteriophage with a viral titre reduction of $10^{7.5}$-fold under visible light irradiation at 0.12 mW cm^{-2} for 40 min.[185] Substituting O^{2-} in TiO_2 with N anions in the crystal lattice of TiO_2 (N-doped TiO_2, $TiO_{2-x}N_x$) generates impurity energy levels above the VB of TiO_2,[216] causing visible light absorption and inactivating MS2 bacteriophage with a viral titre reduction of 10-fold under visible light irradiation at 150 mW cm^{-2} for 5 h.[188] PdO-modified $TiO_{2-x}N_x$ ($PdO/TiO_{2-x}N_x$) with Pd : N : Ti = 0.03 : 0.1 : 1 was deposited on a mesoporous activated carbon fibre template by a sol–gel process along with post-calcination in air at 450 °C for 3 h, which led to inactivation of MS2 bacteriophage with a viral titre reduction of $10^{1.3}$-fold under visible light irradiation at 100 mW cm^{-2} for 1 h.[188]

In addition to various visible-light-responsive TiO_2 photocatalysts, g-C_3N_4, WO_3, $BiWO_4$, and Ag/AgCl with E_g of 2.6–2.7 eV[211,217–219] have been reported to inactivate viruses such as avian influenza virus, goose parvovirus, and MS2 and Qβ bacteriophages.[101,187,190,194,196] The photocatalytic inactivating activity of g-C_3N_4 caused a reduction in viral titre by $>10^{7.5}$-fold for MS2 bacteriophage under visible light irradiation at 150 mW cm^{-2} for 5 h, which is close to the 10^8-fold reduction induced by Ag/AgCl and higher than $>10^{4.2}$- and 10-fold reductions for $BiWO_4$ and $TiO_{2-x}N_x$, respectively.[187] g-C_3N_4 containing deposits of Ag_3PO_4 ($E_g \approx 2.4$ eV, $E_{VB} \approx 2.9$ V)[220] with 200 nm diameter (Ag_3PO_4/g-C_3N_4) inactivated MS2 bacteriophage with a viral titre reduction of $10^{6.5}$-fold under visible light irradiation at 30 mW cm^{-2} for 80 min, which was higher than $10^{3.5}$- and $10^{4.5}$-fold reduction levels achieved with g-C_3N_4 and Ag_3PO_4, respectively.[189] Glass coated with a 80 nm thick film that included WO_3 (15 nm) and graphene (0.9 nm) with a W/C atomic ratio of 1.2 increased viral titre reduction of MS2 bacteriophage by 10^5-fold compared to $10^{0.8}$-fold for WO_3-coated glass under visible light irradiation at 110 mW cm^{-2} for 3 h.[190] Coating materials with WO_3 is now being practically used as a visible-light-response photocatalyst to functionalize high-touch car surfaces with antiviral and antibacterial activity. Glass and polyethylene terephthalate films coated by a composite of WO_3 (100–200 nm) and Pt NPs (3–20 nm) with a Pt weight ratio of 0.03–5% inactivated avian influenza virus (H1N1) and goose parvovirus with viral titre reductions of $10^{3.3}$–$10^{5.5}$ and $10^{2.5}$-fold, respectively, under visible light irradiation at 0.15 mW cm^{-2} for 2 h using a conventional room lamp.[191,192] Although further mechanistic investigation is warranted, it was suggested that generation of $O_2^{\bullet-}$ and H_2O_2 from the reduction of O_2 in the presence of H_2O by photogenerated electrons, and hot electrons by surface plasmon resonance (SPR) excitation of AgNPs provided the reactive species for

g-C_3N_4 (E_{CB} = −1.3 V),[221] WO_3 (E_{CB} = 0.5 V),[222,223] and Ag/AgCl,[219] respectively.

TiO_2 is mostly used as a UV photocatalyst to inactivate viruses under UV light irradiation at 0.01–3 mW cm^{-2}. On the other hand, various materials have been studied as visible-light-responsive photocatalysts to inactivate viruses at 100–150 mW cm^{-2}. Interestingly, Cu_xO/TiO_2 (Cu^+/Cu^{2+} = 0.13) and Pt/WO_3 inactivate viruses under visible light irradiation using white incandescent lamps and white LEDs at 0.022–0.15 mW cm^{-2}.

4.3. Visible light-driven triplet photosensitizer-coated surfaces

Triplet photosensitizers such as benzophenones, porphyrins, boron dipyrromethenes (BODIPY), and fullerene (C_{60}) can generate $^1O_2$ through triplet–triplet energy transfer from triplet-excited photosensitizers to O_2 with $E(^1\Sigma–^3\Sigma)$ = 1.63 eV[175,224,225] to inactivate viruses under light irradiation (Table 4 and Fig. 10). For example, 5,10,15,20-tetrakis(1-methylpyridinium-4-yl)porphyrin (TMPyP) (λ_{max} = 441 nm (2.81 eV), $E_{triplet}$ = 1.88 eV)[226] and 2,6-diiodo-1,3,5,7-tetramethyl-8-(*N*-methyl-4-pyridyl)-4,4′-difluoroboradiazaindacene (DIMPy-BODIPY) (λ_{max} = 546 nm (2.27 eV), $E_{triplet}$ = 2.10 eV)[193] were embedded by electrospinning into polyacrylonitrile (PAN) nanofibers to inactivate viruses such as vesicular stomatitis virus and human adenovirus-5 with viral titre reductions of 10^5- and 10^4-fold, respectively, under visible light irradiation at 65 mW cm^{-2} for 1 and 0.5 h.[193] Poly(vinyl alcohol-*co*-ethylene) (PVA-*co*-PE) nanofiber membranes prepared by electrospinning, followed by covalent bonding of benzophenones and polyphenols as triplet photosensitizers (λ_{max} = 332 nm (3.73 eV)) inactivated T7 bacteriophage (a non-enveloped virus) with a viral titre reduction of 10^5-fold under daylight irradiation (300–800 nm) at 6.5 mW cm^{-2} for 5 min.[196] C_{60} (λ_{onset} = 661 and 408 nm (1.88 and 3.04 eV, respectively), $E_{triplet}$ = 1.5–2.2 eV)[227–229] inactivated Semliki forest virus and vesicular stomatitis virus with viral titre reductions of around 10^7-fold in both cases under 495 nm light irradiation at 29.4 mW cm^{-2} for 6 h,[197] while the reduction was $10^{1.7}$-fold for MS2 bacteriophage on a stainless steel mesh coated with composites of C_{60} and amine-modified SiO_2 under 470 nm light irradiation at 18.8 mW cm^{-2} for 1.5 h.[198] Triplet photosensitizers such as benzophenones, porphyrins, and BODIPY are damaged through photobleaching by oxidative reactions with $^1O_2$ that is generated during triplet photosensitized reactions. It is noted that C_{60} shows higher photostability with a weaker absorption coefficient of 710 M^{-1} cm^{-1} at 536 nm[228] than (1–5) × 10^5 and (4–10) × 10^4 M^{-1} cm^{-1} at 400–450 nm and 530–570 nm for porphyrins[230] and BODIPY,[231] respectively. Together, these results outline key design parameters, including strong absorption coefficient, high yield of the triplet-state and $^1O_2$ generation, and high photostability, that are required for visible-light-responsive triplet photosensitizers to exhibit high levels of virus-inactivating activity.

5. SARS-CoV-2 inactivation

SARS-CoV-2 is an enveloped virus with a single positive-stranded RNA genome. Current findings support that SARS-CoV-2 is highly stable at 4 °C with only a $10^{0.7}$-fold reduction of viral titre after 14 days at that temperature.[75] Such findings highlight the critical need for disinfecting surfaces to mitigate potential spreading of SARS-CoV-2. Both UV irradiation and chemicals such as hypochlorite, H_2O_2, ethanol, and a commercial QAC have been demonstrated to reduce the viral titre of SARS-CoV-2 by 10^3–10^5-fold.[86–92] Ozone is a strong oxidant and widely used for disinfection of water, air, and surfaces, and ozone treatment in hospitals is increasingly used during the ongoing COVID-19 pandemic. Ozone is suggested by molecular modelling to react with specific amino acids and lipid components found in the proteins and lipid bilayer envelope of SARS-CoV-2 virus particles, respectively.[232] In addition to disinfecting surfaces with UV irradiation and chemicals, antiviral material-coated surfaces have been studied for SARS-CoV-2 inactivation.

The inactivation of SARS-CoV-2 on antiviral material-coated surfaces is summarized in Table 5. AgNP-coated non-woven fabric masks and polycotton fabrics have been found to be effective in inhibiting SARS-CoV-2 with a reduction of infectious virus number by approximately 83–99%.[233,234] An antiviral test of AgNPs with different sizes ranging from 2 to 100 nm showed that the infectious amount of SARS-CoV-2 was reduced by

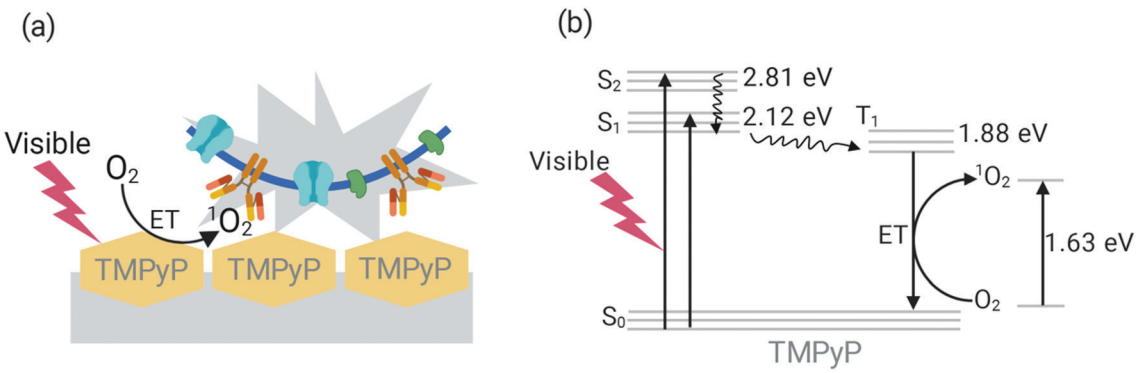

Fig. 10 Virus inactivation on surfaces coated with 5,10,15,20-tetrakis(1-methylpyridinium-4-yl)porphyrin (TMPyP) as a triplet photosensitizer under visible light irradiation (a). $^1O_2$ is generated from triplet–triplet energy transfer (ET) (b), causing the oxidative degradation of molecular components within virus particles.

Table 5 Inactivation of SARS-CoV-2 on antiviral material-coated surfaces

Antiviral material	Initial viral titre (N_0)	Virus reduction ratio, $\log_{10}(N_0/N_t)$ (exposure time)	Ref.
AgNPs (2 nm, 2 mg L^{-1})	1.3×10^9 RNA copies	99.2%, 2.1 (1 h)	235
AgNPs (10 nm, 2 mg L^{-1})	1.3×10^9 RNA copies	92.3%, 1.1 (1 h)	235
AgNPs (15 nm, 2 mg L^{-1})	1.3×10^9 RNA copies	90%, 1.0 (1 h)	235
AgNPs (50 nm, 2 mg L^{-1})	1.3×10^9 RNA copies	38.5%, 0.21 (1 h)	235
AgNPs (80 nm, 2 mg L^{-1})	1.3×10^9 RNA copies	53.9%, 0.27 (1 h)	235
AgNPs (100 nm, 2 mg L^{-1})	1.3×10^9 RNA copies	61.5%, 0.41 (1 h)	235
Ag nanocluster (0.55 at%)/silica composite-coated mask	2.1×10^4 $TCID_{50}$ mL^{-1}	91.9%, 1.1 (1.5 h)	234
Ag nanocluster (1.53 at%)/silica composite-coated mask	2.9×10^4 $TCID_{50}$ mL^{-1}	>99.9%, >4 (1.5 h)	234
AgNPs (23.5 nm, 5%)-coated polycotton	1.26×10^9 copies mL^{-1}	83.1%, 0.77(5 min)	233
Metallic Ag (2 mm) and Zn (1 mm) dot-coated polyester fabric	10^5 particles mL^{-1} 10^5 particles mL^{-1}	60%, 0.40 (1 min) 75%, 0.60 (5 min)	236
Clyraguard cuprous iodine complex	10^6 $TCID_{50}$ mL^{-1}	99.9%, >4 (0.5 h)	250
Annealed Cu (5–60 μm)-coated stainless-steel	$10^{5.1}$ $TCID_{50}$ mL^{-1}	97.9%, 1.8 (5 h)	251
Cu (5–60 μm)-coated stainless-steel	$10^{4.9}$ $TCID_{50}$ mL^{-1}	99.2%, 1.9 (5 h)	251
Cu powder (0.8 ± 1.0 μm)	$10^{5.0}$ PFU mL^{-1}	99.8%, >2.7 (10 min)	239
Luminore CopperTouch™ (85% Cu)	1.3×10^5 PFU mL^{-1}	99.8%, 2.8 (2 h)	252
Cu_2O/PU-coated glass	$10^{7.8}$ $TCID_{50}$ mL^{-1}	99.9%, >3.64 (1 h)	237
Cu_2O/PU-coated stainless steel	$10^{7.8}$ $TCID_{50}$ mL^{-1}	99.9%, 2.97 (1 h)	237
CuO (30 μm)-coated glass	$10^{7.8}$ $TCID_{50}$ mL^{-1}	99.9%, 3.1 (1 h)	238
Si_3N_4 powder (0.8 ± 1.0 μm)	$10^{5.0}$ $TCID_{50}$	>99.9%, >3.0 (10 min)	239
Aluminium nitride powder (1.2 ± 0.6 μm)	$10^{5.0}$ $TCID_{50}$	>99.9%, >3.7 (10 min)	239
Etched Al alloy with nanostructured surface (R_{rms} = 995 ± 115 nm)	10^5 $TCID_{50}$ mL^{-1}	>99.9%, 5 (6 h)	242
Zn^{2+} (0.033%)-embedded PA66 fabric	10^4 PFU mL^{-1}	90%, 2 (1 h)	169

90–99% after 1 h exposure to 2 mg L^{-1} AgNPs with nanoparticle diameters ranging from 2 to 15 nm, while the corresponding reduction levels were 38–62% for AgNPs with diameters ranging from 50 to 100 nm.[235] A luciferase-based pseudovirus entry assay revealed that AgNPs potently inhibited viral entry step *via* disrupting viral integrity. However, cytotoxic effects were observed for AgNPs at concentrations of $\geq$20 mg L^{-1}, indicating that improper disposal of Ag-containing products could harm environmental ecosystems. An electroceutical polyester fabric containing Ag and Zn metal dots generated a potential difference of 0.5 V, which resulted in 60–75% inactivation of a model porcine respiratory coronavirus after contact for 1–5 min.[236]

Glass and stainless steel coated with a PU film with a thickness of 10–16 μm that contained 5.1 μm Cu_2O particles reduced the viral titre by $>10^{3.64}$- and $10^{2.97}$-fold after contact for 1 h, as compared to a reduction of only $10^{0.04}$-fold for uncoated surfaces.[237] Glass coated with 30 μm CuO reduced SARS-CoV-2 viral titre by $10^{3.1}$-fold after contact for 1 h, and the coating remained durable even after exposure to 70% ethanol or 3 wt% bleach.[238] A 15 min exposure to 15 wt% aqueous suspensions of Cu particles, silicon nitride (Si_3N_4), or aluminium nitride (AlN) showed >99% viral inactivation of SARS-CoV-2 virus particles as well as degradation of viral RNA.[239] The antiviral effect of Si_3N_4 and AlN may be related to the leaching of N atoms from the surface to form gaseous ammonia (NH_3) and ammonium (NH_4^+) ions through hydrolysis. The similarity between NH_4^+ on Si_3N_4 and the N-terminal of lysine might trigger an effective "competitive binding" mechanism for SARS-CoV-2 virus particle inactivation,[240] while eluted NH_3 may penetrate to the inside of virus particles and degrade viral RNA through alkaline trans-esterification *via* hydrolysis of phosphodiester bonds in the nucleic acid structure.[241] Notably, the fabrication of Al alloy surfaces with randomly aligned ridges with 23 nm separation distance reduced the SARS-CoV-2 viral titre by 10^5-fold after contact for 6 h compared to a flat Al surface,[242] highlighting the importance of nanostructure design.

In addition to the antiviral surfaces described above, self-cleaning surfaces coated by other antiviral materials such as QACs, metal ions, visible-light-responsive photocatalysts, and triplet photosensitizers for other enveloped viruses can also be examined for decontamination of SARS-CoV-2 due to the similarity among enveloped virus particle structures.[243,244] It is noted that envelope proteins, such as the S protein of SARS-CoV-2, are generally amphipathic[245,246] and negatively charged at physiological pH,[247,248] and possess several disulphide bonds.[38,249] For example, the Cys15–Cys136 and Cys840–Cys851 disulphide pairs are found in the SARS-CoV-2 S protein and important for protein folding.[48] Thus, both positively charged and hydrophobic groups on antiviral surfaces can interact with viral envelope proteins and trigger morphological/conformational changes,[32,33] while AgNPs, CuNPs, and Au and Cu compounds can in principle inhibit S protein-mediated envelope fusion. Interestingly, the coating of contact surfaces in cars by WO_3 as a visible-light-responsive photocatalyst is increasing during the COVID-19 pandemic, highlighting the potential for suitable material innovations to be readily deployed once appropriate standards for durability, cost, and scalability are demonstrated among various technical objectives.

6. Conclusions and outlook

Viruses can contaminate surfaces and survive in inanimate environments, although they cannot replicate independently without a host cell. Temperature, humidity, and surface properties influence the duration and degree of virus survival. As temperature

Table 6 Comparison of typical self-cleaning surfaces for decontamination of viruses[a]

Self-cleaning surface	Mechanism	Challenges	Future opportunities
SHPB	Repel by "air cushion" between water and SHPB surface[94,99]	Incomplete detachment with viral titre reduction of $\leq 10^2$-fold, low durability due to rubbing	Combine with antiviral materials and guide nanostructure fabrication
QAC-coated	Disrupt PL layer of envelopes by electrostatic and hydrophobic interactions[107,108,124–126]	No or less antiviral activity against non-enveloped (NE) viruses with viral titre reduction of $<10^{0.5}$-fold for 2 h	Combine with ROS-inducing antiviral materials
Ag^+- or AgNP-coated	Disrupt SH/S–S exchange of envelope proteins by Ag^+;[109–111] oxidize proteins by ROS generated from reduction of O_2 by Ag^0[148,156,157]	High cost of Ag, no or less antiviral activity against NE viruses with viral titre reduction of $<10^{1.5}$-fold for 1 h	Develop AgNP-coated surfaces with high Ag content and low leaching
Cu^{2+}-coated	Disrupt SH/S–S exchange of envelope proteins and viral nucleic acid degradation by Cu^{2+}[109,113,114,162,163]	No or less antiviral activity against NE viruses with viral titre reduction of $<10^{0.5}$-fold for 0.5–4 h	Develop composites of CuO and Cu, and/or combine with ROS-mediated antiviral materials
Cu or Cu^+ compound-coated	Oxidize proteins by ROS generated from reduction of O_2 by Cu^+ and disrupt SH/S–S exchange of envelope proteins by Cu^+[119,122,164,166]	Short-time antiviral activity of Cu^+ as active species released from Cu and Cu^+ compounds at high humidity	Coat surface with 10–50 nm thick polymer films containing firmly attached Cu and Cu_2O particles
Photocatalyst-coated	Degrade envelope and capsid proteins during TiO_2 photocatalysis[200,201]	Low inactivating activity under visible light irradiation	Modulate doping, defects, and vacancies of TiO_2 to increase inactivating activity
Visible-light-responsive photocatalyst-coated	Degrade proteins on envelope and capsid during photocatalysis[185–188,190,216]	Requires strong light excitation intensity of 100–150 mW cm^{-2}, low inactivating activity	Identify/design photocatalysts with strong absorption and high activity
Visible-light-driven photosensitizer-coated	Degrade proteins on envelope and capsid by $^1O_2$ generated from triplet photosensitizer[193,197,198]	Photobleaching of photosensitizer, low inactivating activity	Combine with polymer nanofiber membranes and identify/design photosensitizers with strong absorption and high activity

[a] Summarized from Tables 2–4.

decreases at moderate humidity (40–70%), viruses typically survive for longer periods of time. The exposure of viruses to cold air outdoors and dry air indoors tends to increase virus transmission and spreading, which is consistent with COVID-19 transmission rates observed in various countries worldwide and the generally occurring seasonal flu in winter months.[253,254] Therefore, the development of self-cleaning surfaces for virus decontamination by inactivation mechanisms is urgently needed as summarized in Table 6.

Although the anti-adhesion property of SHPB surfaces with nanostructures disappears by rubbing, the self-healing and antiviral properties of anti-adhesion surfaces can improve durability and performance reliability. To date, a variety of antiviral surfaces have been prepared to inactivate viruses. For example, QAC-coated surfaces inactivate enveloped viruses but not non-enveloped viruses. In general, Cu-coated surfaces have received more attention than Ag-coated surfaces, due to the lower cost of Cu and related broad-spectrum antiviral activity against both enveloped and non-enveloped viruses. On the other hand, a TiO_2 photocatalyst on surfaces can inactivate viruses and can be used in air filters and membrane-based water filters for virus decontamination under UV light irradiation. Visible-light-responsive photocatalyst nanofiber membranes can also inactivate viruses under visible light irradiation.

Looking forward, the development of broadly useful antiviral surface coatings that work against multiple viruses would be beneficial to deal with current virus problems and future ones. From this perspective, ROS-mediated oxidation is likely the best inactivation method for developing improved antiviral surface coatings, especially those that utilize Cu and Cu^+ compounds.[255,256] Since stainless steel is widely used in hospitals and public facilities, coating steel surfaces with Cu and Cu^+ compounds can create self-cleaning properties for virus inactivation.[257,258] While Cu-based coatings are widely used, an important need remains to develop practically useful nanostructured Cu arrays and nanoporous Cu_2O, which can potentially improve viral inactivation performance to a significant extent. In addition to empirical results supporting this notion, the design of nanoporous surfaces also fits with fluid mechanic models.[259]

Fig. 11 presents illustrative examples of future design directions that could be useful to explore for next-generation antiviral surface coatings. Ultimately, improving performance results will depend

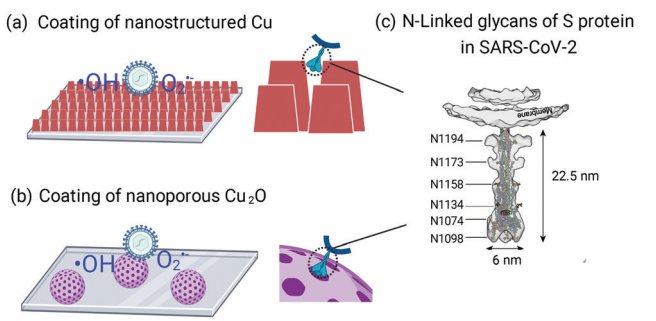

Fig. 11 Possible directions for designing improved antiviral surface coatings. The examples focus on tuning nanostructure geometry and include nanostructured Cu arrays (a) and nanoporous Cu_2O (b) to optimize viral protein-surface contact, thereby increasing the impact of ROS-mediated oxidation. Postfusion S protein structure of SARS-CoV-2 fitted with Protein Data Bank ID of 6XRA and showing densities of N1098, N1074, N1134, N1158, N1173, and N1194 *N*-glycosylation sites (c).[37]

on various factors such as surface properties, material structure, antiviral materials, preparation method, environment, and virus type and amount. There is still limited mechanistic understanding about how virus-repelling and virus-inactivating surfaces prevent contamination and facilitate decontamination and further investigation is needed, especially if such efforts can be aligned with functional design concepts such as nanoarchitectonics.[260,261]

While Cu-based coatings are already widely used in real-life settings, most of the advanced material surface coatings described herein have not yet been commercialized. Interdisciplinary research across the fields of virology, chemistry, physics, materials science, surface science, nanotechnology, polymer science, and engineering could further enhance ongoing material innovation in the field and support the development of high-performing, next-generation antiviral surface coatings for practical use and broad application. One promising application scope involves antiviral face masks, including photoactive coatings[262] and natural material-based coatings with improved biocompatibility,[263] and can be combined with emerging topics such as stimuli-responsive materials,[264,265] biomimetic surface functionalization,[266] and advanced nanomaterials, *e.g.*, two-dimensional materials.[267]

Conflicts of interest

There are no conflicts to declare.

Acknowledgements

This work was supported by the National Natural Science Foundation of China (No. 21976063) and ''1000 Foreign Experts Program'' of the Chinese State Administration of Foreign Experts Affairs (No. WQ2017420438) as well as by the National Research Foundation of Korea (NRF) grant funded by the Korean government (MSIT) (No. 2020R1C1C1004385). In addition, this work was supported by the Brain Pool Program through the National Research Foundation of Korea (NRF) funded by the Ministry of Science and ICT (2019H1D3A1A01070318). Figure illustrations were created with BioRender.com under an academic lab subscription.

Notes and references

1 I. Schröder, *ACS Chem. Health Saf.*, 2020, **27**, 160–169.
2 E. E. A. Osman, P. L. Toogood and N. Neamati, *ACS Infect. Dis.*, 2020, **6**, 1548–1552.
3 H. Huang, C. Fan, M. Li, H. L. Nie, F. B. Wang, H. Wang, R. Wang, J. Xia, X. Zheng, X. Zuo and J. Huang, *ACS Nano*, 2020, **14**, 3747–3754.
4 F. S. Dawood, A. D. Iuliano, C. Reed, M. I. Meltzer, D. K. Shay, P.-Y. Cheng, D. Bandaranayake, R. F. Breiman, W. A. Brooks, P. Buchy, D. R. Feikin, K. B. Fowler, A. Gordon, N. T. Hien, P. Horby, Q. S. Huang, M. A. Katz, A. Krishnan, R. Lal, J. M. Montgomery, K. Mølbak, R. Pebody, A. M. Presanis, H. Razuri, A. Steens, Y. O. Tinoco, J. Wallinga, H. Yu, S. Vong, J. Bresee and M.-A. Widdowson, *Lancet Infect. Dis.*, 2012, **12**, 687–695.
5 K. R. Victory, F. Coronado, S. O. Ifono, T. Soropogui and B. A. Dahl, *Morb. Mortal. Wkly. Rep.*, 2015, **64**, 386.
6 O. Cenciarelli, V. Gabbarini, S. Pietropaoli, A. Malizia, A. Tamburrini, G. M. Ludovici, M. Carestia, D. Di Giovanni, A. Sassolini, L. Palombi, C. Bellecci and P. Gaudio, *Virus Res.*, 2015, **210**, 318–326.
7 B. K. Yoon, W. Y. Jeon, T. N. Sut, N. J. Cho and J. A. Jackman, *ACS Nano*, 2021, **15**, 125–148.
8 J. H. Kim, F. Marks and J. D. Clemens, *Nat. Med.*, 2021, **27**, 205–211.
9 I. Jones and P. Roy, *Lancet*, 2021, **397**, 642–643.
10 N. Dagan, N. Barda, E. Kepten, O. Miron, S. Perchik, M. A. Katz, M. A. Hernán, M. Lipsitch, B. Reis and R. D. Balicer, *N. Engl. J. Med.*, 2021, **384**, 1412–1423.
11 C. S. Adamson, K. Chibale, R. J. M. Goss, M. Jaspars, D. J. Newman and R. A. Dorrington, *Chem. Soc. Rev.*, 2021, **50**, 3647–3655.
12 S. Pelly and D. Liotta, *ACS Cent. Sci.*, 2021, **7**, 396–399.
13 P. Y. Chia, K. K. Coleman, Y. K. Tan, S. W. X. Ong, M. Gum, S. K. Lau, X. F. Lim, A. S. Lim, S. Sutjipto, P. H. Lee, T. T. Son, B. E. Young, D. K. Milton, G. C. Gray, S. Schuster, T. Barkham, P. P. De, S. Vasoo, M. Chan, B. S. P. Ang, B. H. Tan, Y.-S. Leo, O.-T. Ng, M. S. Y. Wong, K. Marimuthu and for the Singapore Novel Coronavirus Outbreak Research Team, *Nat. Commun.*, 2020, **11**, 2800.
14 J. L. Santarpia, D. N. Rivera, V. L. Herrera, M. J. Morwitzer, H. M. Creager, G. W. Santarpia, K. K. Crown, D. M. Brett-Major, E. R. Schnaubelt, M. J. Broadhurst, J. V. Lawler, S. P. Reid and J. J. Lowe, *Sci. Rep.*, 2020, **10**, 12732.
15 M. Colaneri, E. Seminari, S. Novati, E. Asperges, S. Biscarini, A. Piralla, E. Percivalle, I. Cassaniti, F. Baldanti, R. Bruno, M. U. Mondelli and COVID19 IRCCS San Matteo Pavia Task Force, *Clin. Microbiol. Infect.*, 2020, **26**, 1094.e1–1094.e5.
16 C. Weiss, M. Carriere, L. Fusco, I. Capua, J. A. Regla-Nava, M. Pasquali, J. A. Scott, F. Vitale, M. A. Unal and C. Mattevi, *ACS Nano*, 2020, **14**, 6383–6406.
17 L. Liang, A. Ahamed, L. Ge, X. Fu and G. Lisak, *ChemPlusChem*, 2020, **85**, 2105–2128.
18 D. Chakhalian, R. B. Shultz, C. E. Miles and J. Kohn, *J. Biomed. Mater. Res., Part A*, 2020, **108**, 1974–1990.
19 Z. Tang, N. Kong, X. Zhang, Y. Liu, P. Hu, S. Mou, P. Liljeström, J. Shi, W. Tan, J. S. Kim, Y. Cao, R. Langer, K. W. Leong, O. C. Farokhzad and W. Tao, *Nat. Rev. Mater.*, 2020, **5**, 847–860.
20 B. Balasubramaniam, Prateek, S. Ranjan, M. Saraf, P. Kar, S. P. Singh, V. K. Thakur, A. Singh and R. K. Gupta, *ACS Pharmacol. Transl. Sci.*, 2021, **4**, 8–54.
21 A. Saxena, D. Khare, S. Agrawal, A. Singh and A. K. Dubey, *Emergent Mater.*, 2021, 1–17.
22 J. Yu, C. Kuwentrai, J.-D. Huang and C. Xu, *Biomicrofluidics*, 2021, **15**, 011501.
23 J. A. Jackman, B. K. Yoon, L. Ouyang, N. Wang, A. R. Ferhan, J. Kim, T. Majima and N. J. Cho, *Adv. Funct. Mater.*, 2020, 2008352, DOI: 10.1002/adfm.202008352.

24 B. Song, E. Zhang, X. Han, H. Zhu, Y. Shi and Z. Cao, *ACS Appl. Mater. Interfaces*, 2020, **12**, 21330–21341.
25 Z. Sun and K. Ostrikov, *Sustainable Mater. Technol.*, 2020, e00203.
26 S. Basak and G. Packirisamy, *Nano-Struct. Nano-Objects*, 2020, **24**, 100620.
27 P. K. Rai, Z. Usmani, V. K. Thakur, V. K. Gupta and Y. K. Mishra, *Curr. Res. Green Sustainable Chem.*, 2020, **3**, 100011.
28 S. M. Imani, L. Ladouceur, T. Marshall, R. Maclachlan, L. Soleymani and T. F. Didar, *ACS Nano*, 2020, **14**, 12341–12369.
29 P. Erkoc and F. Ulucan-Karnak, *Prosthesis*, 2021, **3**, 25–52.
30 S. Mallakpour, E. Azadi and C. M. Hussain, *New J. Chem.*, 2021, **45**, 6167–6179.
31 M. Zare, M. Sillanpää and S. Ramakrishna, *Mater. Adv.*, 2021, **2**, 2188–2199.
32 E. Joonaki, A. Hassanpouryouzband, C. L. Heldt and O. Areo, *Chem.*, 2020, **6**, 2135–2146.
33 Y. Xin, G. Grundmeier and A. Keller, *Adv. Nanobiomed Res.*, 2021, **1**, 2000024.
34 N. Castaño, S. C. Cordts, M. Kurosu Jalil, K. S. Zhang, S. Koppaka, A. D. Bick, R. Paul and S. K. Tang, *ACS Omega*, 2021, **6**, 6509–6527.
35 Y. Xin, G. Grundmeier and A. Keller, *Adv. Nanobiomed Res.*, 2021, **1**, 2000024.
36 A. Armanious, M. Aeppli, R. Jacak, D. Refardt, T. Sigstam, T. Kohn and M. Sander, *Environ. Sci. Technol.*, 2016, **50**, 732–743.
37 H. Yao, Y. Song, Y. Chen, N. Wu, J. Xu, C. Sun, J. Zhang, T. Weng, Z. Zhang and Z. Wu, *Cell*, 2020, **183**, 730–738.e713.
38 D. Wrapp, N. Wang, K. S. Corbett, J. A. Goldsmith, C.-L. Hsieh, O. Abiona, B. S. Graham and J. S. McLellan, *Science*, 2020, **367**, 1260–1263.
39 X. Ou, Y. Liu, X. Lei, P. Li, D. Mi, L. Ren, L. Guo, R. Guo, T. Chen and J. Hu, *Nat. Commun.*, 2020, **11**, 1–12.
40 F. Li, *Annu. Rev. Virol.*, 2016, **3**, 237–261.
41 M. Gur, E. Taka, S. Z. Yilmaz, C. Kilinc, U. Aktas and M. Golcuk, *J. Chem. Phys.*, 2020, **153**, 075101.
42 S. L. Warnes, Z. R. Little and C. W. Keevil, *mBio*, 2015, **6**, e01697-15.
43 T. Labadie, C. Batéjat and J.-C. Manuguerra, *Front. Microbiol.*, 2018, **9**, 1496.
44 J. A. Plante, Y. Liu, J. Liu, H. Xia, B. A. Johnson, K. G. Lokugamage, X. Zhang, A. E. Muruato, J. Zou and C. R. Fontes-Garfias, *Nature*, 2021, **592**, 116–121.
45 B. Xue, D. Blocquel, J. Habchi, A. V. Uversky, L. Kurgan, V. N. Uversky and S. Longhi, *Chem. Rev.*, 2014, **114**, 6880–6911.
46 N. C. Rockey, J. B. Henderson, K. Chin, L. Raskin and K. R. Wigginton, *Environ. Sci. Technol.*, 2021, **55**, 3322–3332.
47 G. Nayak, H. A. Aboubakr, S. M. Goyal and P. J. Bruggeman, *Plasma Processes Polym.*, 2018, **15**, 1700119.
48 Y. Cai, J. Zhang, T. Xiao, H. Peng, S. M. Sterling, R. M. Walsh, S. Rawson, S. Rits-Volloch and B. Chen, *Science*, 2020, **369**, 1586–1592.
49 N. van Doremalen, T. Bushmaker, D. H. Morris, M. G. Holbrook, A. Gamble, B. N. Williamson, A. Tamin, J. L. Harcourt, N. J. Thornburg, S. I. Gerber, J. O. Lloyd-Smith, E. de Wit and V. J. Munster, *N. Engl. J. Med.*, 2020, **382**, 1564–1567.
50 R. Fischer, S. Judson, K. Miazgowicz, T. Bushmaker, J. Prescott and V. J. Munster, *Emerging Infect. Dis.*, 2015, **21**, 1243–1246.
51 L. M. Casanova, S. Jeon, W. A. Rutala, D. J. Weber and M. D. Sobsey, *Appl. Environ. Microbiol.*, 2010, **76**, 2712–2717.
52 J. O. Noyce, H. Michels and C. W. Keevil, *Appl. Environ. Microbiol.*, 2007, **73**, 2748–2750.
53 M. Y. Y. Lai, P. K. C. Cheng and W. W. L. Lim, *Clin. Infect. Dis.*, 2005, **41**, e67–e71.
54 S. J. Kim, J. Si, J. E. Lee and G. Ko, *Environ. Sci. Technol.*, 2012, **46**, 13303–13310.
55 H. F. Rabenau, J. Cinatl, B. Morgenstern, G. Bauer, W. Preiser and H. W. Doerr, *Med. Microbiol. Immunol.*, 2005, **194**, 1–6.
56 A. S. Jureka, J. A. Silvas and C. F. Basler, *Viruses*, 2020, **12**, 622.
57 S. Firquet, S. Beaujard, P.-E. Lobert, F. Sané, D. Caloone, D. Izard and D. Hober, *Microbes Environ.*, 2015, ME14145.
58 M. Hernando-Pérez, A. Cartagena-Rivera, A. L. Božič, P. J. Carrillo, C. San Martín, M. G. Mateu, A. Raman, R. Podgornik and P. De Pablo, *Nanoscale*, 2015, **7**, 17289–17298.
59 C. V. Chrysikopoulos and V. I. Syngouna, *Colloids Surf., B*, 2012, **92**, 74–83.
60 N. Castaño, S. Cordts, M. K. Jalil, K. Zhang, S. Koppaka, A. Bick, R. Paul and S. K. Tang, *arXiv.org, e-Print Arch., Quant. Biol.*, 2020.
61 S. B. Kasloff, A. Leung, J. E. Strong, D. Funk and T. Cutts, *Sci. Rep.*, 2021, **11**, 984.
62 S. Chatterjee, J. S. Murallidharan, A. Agrawal and R. Bhardwaj, *Phys. Fluids*, 2021, **33**, 021701.
63 P. Vasickova, I. Pavlik, M. Verani and A. Carducci, *Food Environ. Virol.*, 2010, **2**, 24–34.
64 J. Hasan, Y. Xu, T. Yarlagadda, M. Schuetz, K. Spann and P. K. D. V. Yarlagadda, *ACS Biomater. Sci. Eng.*, 2020, **6**, 3608–3618.
65 G. Grass, C. Rensing and M. Solioz, *Appl. Environ. Microbiol.*, 2011, **77**, 1541–1547.
66 L. Zhao, Y. Qi, P. Luzzatto-Fegiz, Y. Cui and Y. Zhu, *Nano Lett.*, 2020, **20**, 7744–7750.
67 P. Mecenas, R. T. D. R. M. Bastos, A. C. R. Vallinoto and D. Normando, *PLoS One*, 2020, **15**, e0238339.
68 J. W. Tang, *J. R. Soc., Interface*, 2009, **6**, S737–746.
69 A. J. Prussin, D. O. Schwake, K. Lin, D. L. Gallagher, L. Buttling, L. C. Marr and D. W. Schaffner, *Appl. Environ. Microbiol.*, 2018, **84**, e00551–00518.
70 K. H. Chan, J. S. M. Peiris, S. Y. Lam, L. L. M. Poon, K. Y. Yuen and W. H. Seto, *Adv. Virol.*, 2011, **7**, 734690.
71 J. N. Mbithi, V. S. Springthorpe and S. A. Sattar, *Appl. Environ. Microbiol.*, 1991, **57**, 1394–1399.
72 C. S. Cox, *Origins Life Evol. Biospheres*, 1993, **23**, 29–36.
73 S. S. Thompson, M. Flury, M. V. Yates and W. A. Jury, *Appl. Environ. Microbiol.*, 1998, **64**, 304–309.
74 S. Ratnesar-Shumate, G. Williams, B. Green, M. Krause, B. Holland, S. Wood, J. Bohannon, J. Boydston, D. Freeburger,

I. Hooper, K. Beck, J. Yeager, L. A. Altamura, J. Biryukov, J. Yolitz, M. Schuit, V. Wahl, M. Hevey and P. Dabisch, *J. Infect. Dis.*, 2020, **222**, 214–222.
75 A. W. H. Chin, J. T. S. Chu, M. R. A. Perera, K. P. Y. Hui, H.-L. Yen, M. C. W. Chan, M. Peiris and L. L. M. Poon, *Lancet Microbe*, 2020, **1**, e10.
76 J. Biryukov, J. A. Boydston, R. A. Dunning, J. J. Yeager, S. Wood, A. L. Reese, A. Ferris, D. Miller, W. Weaver, N. E. Zeitouni, A. Phillips, D. Freeburger, I. Hooper, S. Ratnesar-Shumate, J. Yolitz, M. Krause, G. Williams, D. G. Dawson, A. Herzog, P. Dabisch, V. Wahl, M. C. Hevey and L. A. Altamura, *mSphere*, 2020, **5**, e00441-20.
77 S. Riddell, S. Goldie, A. Hill, D. Eagles and T. W. Drew, *Virol. J.*, 2020, **17**, 145.
78 Y. W. Choi, A. W. Richardson, M. Sunderman, M. J. Mladineo, P. H. Keyes, K. C. Hofacre and J. K. Middleton, *Lett. Appl. Microbiol.*, 2021, **72**, 366–374.
79 N. V. Doremalen, T. Bushmaker and V. Munster, *Eurosurveillance*, 2013, **18**, 1–4.
80 J. Oxford, E. N. Berezin, P. Courvalin, D. E. Dwyer, M. Exner, L. A. Jana, M. Kaku, C. Lee, K. Letlape, D. E. Low, T. A. Madani, J. R. Rubino, N. Saini, B. D. Schoub, C. Signorelli, P. M. Tierno and X. Zhong, *Am. J. Infect. Control*, 2014, **42**, 423–425.
81 M. T. Brady, J. Evans and J. Cuartas, *Am. J. Infect. Control*, 1990, **18**, 18–23.
82 D. Leblanc, M.-J. Gagné, É. Poitras and J. Brassard, *Food Microbiol.*, 2019, **84**, 103257.
83 S. W. X. Ong, Y. K. Tan, P. Y. Chia, T. H. Lee, O. T. Ng, M. S. Y. Wong and K. Marimuthu, *J. Am. Med. Assoc.*, 2020, **323**, 1610–1612.
84 A. A. Chughtai, S. Stelzer-Braid, W. Rawlinson, G. Pontivivo, Q. Wang, Y. Pan, D. Zhang, Y. Zhang, L. Li and C. R. MacIntyre, *BMC Infect. Dis.*, 2019, **19**, 491.
85 H. Sakaguchi, K. Wada, J. Kajioka, M. Watanabe, R. Nakano, T. Hirose, H. Ohta and Y. Aizawa, *Environ. Health Prev. Med.*, 2010, **15**, 344–349.
86 C. S. Heilingloh, U. W. Aufderhorst, L. Schipper, U. Dittmer, O. Witzke, D. Yang, X. Zheng, K. Sutter, M. Trilling, M. Alt, E. Steinmann and A. Krawczyk, *Am. J. Infect. Control*, 2020, **48**, 1273–1275.
87 H. Inagaki, A. Saito, H. Sugiyama, T. Okabayashi and S. Fujimoto, *Emerging Microbes Infect.*, 2020, **9**, 1744–1747.
88 S. E. Simmons, R. Carrion, K. J. Alfson, H. M. Staples, C. Jinadatha, W. R. Jarvis, P. Sampathkumar, R. F. Chemaly, F. Khawaja, M. Povroznik, S. Jackson, K. S. Kaye, R. M. Rodriguez and M. A. Stibich, *Infect. Control Hosp. Epidemiol.*, 2020, 1–4, DOI: 10.1017/ice.2020.399.
89 J. S. Smith, H. Hanseler, J. Welle, R. Rattray, M. Campbell, T. Brotherton, T. Moudgil, T. F. Pack, K. Wegmann, S. Jensen, J. S. Jin, C. B. Bifulco, S. A. Prahl, B. A. Fox and N. L. Stucky, *Clin. Transl. Sci.*, 2020, e10.
90 V. S. Springthorpe and S. Sattar, *Crit. Rev. Environ. Sci. Technol.*, 1990, **20**, 169–229.
91 A. S. Bidra, J. S. Pelletier, J. B. Westover, S. Frank, S. M. Brown and B. Tessema, *J. Prosthodont.*, 2020, 5, DOI: 10.1111/jopr.13220.
92 J. L. Welch, J. Xiang, S. R. Mackin, S. Perlman, P. Thorne, P. O'Shaughnessy, B. Strzelecki, P. Aubin, M. Ortiz-Hernandez and J. T. Stapleton, *Infect. Control Hosp. Epidemiol.*, 2020, 1–8, DOI: 10.1017/ice.2020.417.
93 J. Zhao, L. Song, J. Yin and W. Ming, *Chem. Commun.*, 2013, **49**, 9191–9193.
94 A. J. Galante, S. Haghanifar, E. G. Romanowski, R. M. Q. Shanks and P. W. Leu, *ACS Appl. Mater. Interfaces*, 2020, **12**, 22120–22128.
95 A. Lafuma and D. Quere, *Nat. Mater.*, 2003, **2**, 457–460.
96 Z. Li and Z. Guo, *Nanoscale*, 2019, **11**, 22636–22663.
97 J. Jiang, H. Zhang, W. He, T. Li, H. Li, P. Liu, M. Liu, Z. Wang, Z. Wang and X. Yao, *ACS Appl. Mater. Interfaces*, 2017, **9**, 6599–6608.
98 E. G. Shafrin and W. A. Zisman, *J. Phys. Chem.*, 1960, **64**, 519–524.
99 I. Mannelli, R. Reigada, I. Suarez, D. Janner, A. Carrilero, P. Mazumder, F. Sagues, V. Pruneri and M. Lakadamyali, *ACS Appl. Mater. Interfaces*, 2016, **8**, 15058–15066.
100 J. Haldar, D. An, L. A. de Cienfuegos, J. Chen and A. M. Klibanov, *Proc. Natl. Acad. Sci. U. S. A.*, 2006, **103**, 17667–17671.
101 S. L. Stanley, F. Scholle, J. D. Zhu, Y. Lu, X. W. Zhang, X. C. Situ and R. A. Ghiladi, *Nanomaterials*, 2016, **6**, 14.
102 R. Nakano, H. Ishiguro, Y. Yao, J. Kajioka, A. Fujishima, K. Sunada, M. Minoshima, K. Hashimoto and Y. Kubota, *Photochem. Photobiol. Sci.*, 2012, **11**, 1293–1298.
103 Y. Mori, T. Ono, Y. Miyahira, V. Q. Nguyen, T. Matsui and M. Ishihara, *Nanoscale Res. Lett.*, 2013, **8**, 93.
104 L. P. Arendsen, R. Thakar and A. H. Sultan, *Clin. Microbiol. Rev.*, 2019, **32**, e00125-18.
105 J. M. Mazurkow, N. S. Yuzbasi, K. W. Domagala, S. Pfeiffer, D. Kata and T. Graule, *Environ. Sci. Technol.*, 2020, **54**, 1214–1222.
106 Q. Lin, J. Y. C. Lim, K. Xue, P. Y. M. Yew and X. J. Loh, *View*, 2020, **1**, e16.
107 B. B. Hsu, S. Yinn Wong, P. T. Hammond, J. Chen and A. M. Klibanov, *Proc. Natl. Acad. Sci. U. S. A.*, 2011, **108**, 61–66.
108 H. Liu, I. Elkin, J. Chen and A. M. Klibanov, *Biomacromolecules*, 2015, **16**, 351–356.
109 I. M. Klotz and B. J. Campbell, *Arch. Biochem. Biophys.*, 1962, **96**, 92–99.
110 R. Cecil and P. J. Mc, *Biochem. J.*, 1957, **66**, 538–543.
111 S. Y. Liau, D. C. Read, W. J. Pugh, J. R. Furr and A. D. Russell, *Lett. Appl. Microbiol.*, 1997, **25**, 279–283.
112 L. Pecci, G. Montefoschi, G. Musci and D. Cavallini, *Amino Acids*, 1997, **13**, 355–367.
113 J. Hodek, V. Zajicova, I. Lovetinska-Slamborova, I. Stibor, J. Mullerova and J. Weber, *BMC Microbiol.*, 2016, **16**, 56.
114 K. Imai, H. Ogawa, V. N. Bui, H. Inoue, J. Fukuda, M. Ohba, Y. Yamamoto and K. Nakamura, *Antiviral Res.*, 2012, **93**, 225–233.
115 S. Zerbib, L. Vallet, A. Muggeo, C. de Champs, A. Lefebvre, D. Jolly and L. Kanagaratnam, *J. Am. Med. Dir. Assoc.*, 2020, **21**, 68–71.e61.

116 M. Minoshima, Y. Lu, T. Kimura, R. Nakano, H. Ishiguro, Y. Kubota, K. Hashimoto and K. Sunada, *J. Hazard. Mater.*, 2016, **312**, 1–7.
117 H. H. Lara, N. V. Ayala-Nuñez, L. Ixtepan-Turrent and C. Rodriguez-Padilla, *J. Nanobiotechnol.*, 2010, **8**, 1–10.
118 K. Sunada, M. Minoshima and K. Hashimoto, *J. Hazard. Mater.*, 2012, **235–236**, 265–270.
119 N. Shionoiri, T. Sato, Y. Fujimori, T. Nakayama, M. Nemoto, T. Matsunaga and T. Tanaka, *J. Biosci. Bioeng.*, 2012, **113**, 580–586.
120 W. H. Koppenol and J. F. Liebman, *J. Phys. Chem.*, 1984, **88**, 99–101.
121 J. Chevalet, F. Rouelle, L. Gierst and J. P. Lambert, *J. Electroanal. Chem. Interfacial Electrochem.*, 1972, **39**, 201–216.
122 T. Wang, J. Wang and Y. Wu, *Corros. Sci.*, 2015, **97**, 89–99.
123 D. Botequim, J. Maia, M. M. Lino, L. M. Lopes, P. N. Simoes, L. M. Ilharco and L. Ferreira, *Langmuir*, 2012, **28**, 7646–7656.
124 E. Tuladhar, M. C. de Koning, I. Fundeanu, R. Beumer and E. Duizer, *Appl. Environ. Microbiol.*, 2012, **78**, 2456–2458.
125 A. M. Larson, B. B. Hsu, D. Rautaray, J. Haldar, J. Chen and A. M. Klibanov, *Biotechnol. Bioeng.*, 2011, **108**, 720–723.
126 J. Haldar, A. K. Weight and A. M. Klibanov, *Nat. Protoc.*, 2007, **2**, 2412–2417.
127 P. A. Fulmer and J. H. Wynne, *ACS Appl. Mater. Interfaces*, 2011, **3**, 2878–2884.
128 S. Klein, M. Cortese, S. L. Winter, M. Wachsmuth-Melm, C. J. Neufeldt, B. Cerikan, M. L. Stanifer, S. Boulant, R. Bartenschlager and P. Chlanda, *Nat. Commun.*, 2020, **11**, 1–10.
129 Y. Hu and L. Sun, *ACS Infect. Dis.*, 2019, **5**, 1070–1080.
130 P. J. P. Carrillo, M. Medrano, A. Valbuena, A. Rodríguez-Huete, M. Castellanos, R. Perez and M. G. Mateu, *ACS Nano*, 2017, **11**, 2194–2208.
131 P. T. Ivanova, D. S. Myers, S. B. Milne, J. L. McClaren, P. G. Thomas and H. A. Brown, *ACS Infect. Dis.*, 2015, **1**, 435–442.
132 Z. Chen, X. Sun, Y. Shen, H. Ni, S. Chai, Q. Zou, X. Zhang and J. Zhang, *Mater. Sci. Eng., C*, 2015, **49**, 234–242.
133 Y. Watanabe, H. Kakehi and Y. Shutoe, *US Pat.*, US10550274B2, 2020.
134 M. Coates, D. W. Connell and D. M. Barron, *Environ. Sci. Technol.*, 1985, **19**, 628–632.
135 S. Ghosh, R. Mukherjee, D. Basak and J. Haldar, *ACS Appl. Mater. Interfaces*, 2020, **12**, 27853–27865.
136 H. Han, J. Wu, C. W. Avery, M. Mizutani, X. Jiang, M. Kamigaito, Z. Chen, C. Xi and K. Kuroda, *Langmuir*, 2011, **27**, 4010–4019.
137 B. B. Hsu and A. M. Klibanov, *Biomacromolecules*, 2011, **12**, 6–9.
138 K. Horie, H. Ando and I. Mita, *Macromolecules*, 1987, **20**, 54–58.
139 A. M. Klibanov, *J. Mater. Chem.*, 2007, **17**, 2479–2482.
140 J. Haldar, J. Chen, T. M. Tumpey, L. V. Gubareva and A. M. Klibanov, *Biotechnol. Lett.*, 2008, **30**, 475–479.
141 J. Lin, S. Qiu, K. Lewis and A. M. Klibanov, *Biotechnol. Prog.*, 2002, **18**, 1082–1086.
142 V. P. Dhende, S. Samanta, D. M. Jones, I. R. Hardin and J. Locklin, *ACS Appl. Mater. Interfaces*, 2011, **3**, 2830–2837.
143 T. R. Sinclair, A. Patil, B. G. Raza, D. Reurink, S. K. van den Hengel, S. A. Rutjes, A. M. D. Husman, H. D. W. Roesink and W. M. de Vos, *J. Membr. Sci.*, 2019, **570**, 494–503.
144 J. Liu, A. Bartesaghi, M. J. Borgnia, G. Sapiro and S. Subramaniam, *Nature*, 2008, **455**, 109–113.
145 J. L. Elechiguerra, J. L. Burt, J. R. Morones, A. Camacho-Bragado, X. Gao, H. H. Lara and M. J. Yacaman, *J. Nanobiotechnol.*, 2005, **3**, 1–10.
146 S. W. Jaros, J. Krol, B. Bazanow, D. Poradowski, A. Chroszcz, D. S. Nesterov, A. M. Kirillov and P. Smolenski, *Molecules*, 2020, **25**, 2119.
147 T. V. M. Sreekanth, P. C. Nagajyothi, P. Muthuraman, G. Enkhtaivan, S. V. P. Vattikuti, C. O. Tettey, D. H. Kim, J. Shim and K. Yoo, *J. Photochem. Photobiol., B*, 2018, **188**, 6–11.
148 P. L. Taylor, A. L. Ussher and R. E. Burrell, *Biomaterials*, 2006, **26**, 7221–7229.
149 A. Piai, Q. Fu, Y. Cai, F. Ghantous, T. Xiao, M. M. Shaik, H. Peng, S. Rits-Volloch, W. Chen and M. S. Seaman, *Nat. Commun.*, 2020, **11**, 1–12.
150 R. Blumenthal, S. Durell and M. Viard, *J. Biol. Chem.*, 2012, **287**, 40841–40849.
151 I. M. Klotz, G. H. Czerlinski and H. A. Fiess, *J. Am. Chem. Soc.*, 1958, **80**, 2920–2923.
152 Y. N. Slavin, J. Asnis, U. O. Hafeli and H. Bach, *J. Nanobiotechnol.*, 2017, **15**, 65.
153 S. Gurunathan, M. Qasim, Y. Choi, J. T. Do, C. Park, K. Hong, J.-H. Kim and H. Song, *Nanomaterials*, 2020, **10**, 1645.
154 H. H. Lara, E. N. Garza-Treviño, L. Ixtepan-Turrent and D. K. Singh, *J. Nanobiotechnol.*, 2011, **9**, 1–8.
155 S. Nakamura, M. Sato, Y. Sato, N. Ando, T. Takayama, M. Fujita and M. Ishihara, *Int. J. Mol. Sci.*, 2019, **20**, 3620.
156 H. He, X. Dong, M. Yang, Q. Yang, S. Duan, Y. Yu, J. Han, C. Zhang, L. Chen and X. Yang, *Catal. Commun.*, 2004, **5**, 170–172.
157 W. He, Y.-T. Zhou, W. G. Wamer, M. D. Boudreau and J.-J. Yin, *Biomaterials*, 2012, **33**, 7547–7555.
158 S. Park, H. H. Park, S. Y. Kim, S. J. Kim, K. Woo and G. Ko, *Appl. Environ. Microbiol.*, 2014, **80**, 2343–2350.
159 E. M. Marti, C. Methivier and C. M. Pradier, *Langmuir*, 2004, **20**, 10223–10230.
160 J. Srogl, J. Hývl, Á. Révész and D. Schröder, *Chem. Commun.*, 2009, 3463–3465.
161 M. Horie, H. Ogawa, Y. Yoshida, K. Yamada, A. Hara, K. Ozawa, S. Matsuda, C. Mizota, M. Tani, Y. Yamamoto, M. Yamada, K. Nakamura and K. Imai, *Arch. Virol.*, 2008, **153**, 1467–1472.
162 G. Borkow and J. Gabbay, *Curr. Med. Chem.*, 2005, **12**, 2163–2175.
163 J. L. Sagripanti, P. L. Goering and A. Lamanna, *Toxicol. Appl. Pharmacol.*, 1991, **110**, 477–485.
164 A. Rigo, A. Corazza, M. L. di Paolo, M. Rossetto, R. Ugolini and M. Scarpa, *J. Inorg. Biochem.*, 2004, **98**, 1495–1501.
165 R. A. Garza-Lopez, J. J. Kozak and H. B. Gray, *ChemRxiv*, 2020, DOI: 10.3390/molecules25092119.

166 M. J. Davies and R. T. Dean, *Radical-mediated protein oxidation: from chemistry to medicine*, Oxford University Press, Oxford, 1997.
167 G. Borkow, R. W. Sidwell, D. F. Smee, D. L. Barnard, J. D. Morrey, H. H. Lara-Villegas, Y. Shemer-Avni and J. Gabbay, *Antimicrob. Agents Chemother.*, 2007, **51**, 2605–2607.
168 G. Borkow, S. S. Zhou, T. Page and J. Gabbay, *PLoS One*, 2010, **5**, e11295.
169 V. Gopal, B. E. Nilsson-Payant, H. French, J. Y. Siegers, B. R. tenOever, W. S. Yung, M. Hardwick and A. J. W. Te Velthuis, *ACS Appl. Mater. Interfaces*, 2021, **13**, 30317–30325.
170 Y. N. Chen, Y. H. Hsueh, C. T. Hsieh, D. Y. Tzou and P. L. Chang, *Int. J. Environ. Res. Public Health*, 2016, **13**, 430.
171 D. Baram-Pinto, S. Shukla, N. Perkas, A. Gedanken and R. Sarid, *Bioconjugate Chem.*, 2009, **20**, 1497–1502.
172 S. Gaikwad, A. Ingle, A. Gade, M. Rai, A. Falanga, N. Incoronato, L. Russo, S. Galdiero and M. Galdiero, *Int. J. Nanomed.*, 2013, **8**, 4303–4314.
173 Y. Fujimori, T. Sato, T. Hayata, T. Nagao, M. Nakayama, T. Nakayama, R. Sugamata and K. Suzuki, *Appl. Environ. Microbiol.*, 2012, **78**, 951–955.
174 M. Fujihira, Y. Satoh and T. Osa, *Nature*, 1981, **293**, 206–208.
175 S. K. Chattopadhyay, C. V. Kumar and P. K. Das, *J. Phys. Chem.*, 1985, **89**, 670–673.
176 H. Cui, J. Jiang, W. Gu, C. Sun, D. Wu, T. Yang and G. Yang, *Photochem. Photobiol.*, 2010, **86**, 1135–1139.
177 W. Han, P. H. Zhang, W. Cao, D. Yang and X. Yan, *Prog. Biochem. Biophys.*, 2004, **31**, 982–985.
178 K. Shiraki, H. Yamada, Y. Yoshida, A. Ohno, T. Watanabe, T. Watanabe, H. Watanabe, H. Watanabe, M. Yamaguchi, F. Tokuoka, S. Hashimoto, M. Kawamura and N. Adachi, *Aerosol Air Qual. Res.*, 2017, **17**, 2901–2912.
179 D. B. Misstear and L. W. Gill, *J. Photochem. Photobiol., B*, 2012, **107**, 1–8.
180 M. V. Liga, E. L. Bryant, V. L. Colvin and Q. Li, *Water Res.*, 2011, **45**, 535–544.
181 E. W. Moon, H. W. Lee, J. H. Rok and J. H. Ha, *Sci. Total Environ*, 2020, **749**, 141574.
182 G. W. Park, M. Cho, E. L. Cates, D. Lee, B. T. Oh, J. Vinje and J. H. Kim, *J. Photochem. Photobiol., B*, 2014, **140**, 315–320.
183 M. V. Liga, S. J. Maguire-Boyle, H. R. Jafry, A. R. Barron and Q. Li, *Environ. Sci. Technol.*, 2013, **47**, 6463–6470.
184 T. Sato and M. Taya, *Biochem. Eng. J.*, 2006, **28**, 303–308.
185 X. Qiu, M. Miyauchi, K. Sunada, M. Minoshima, M. Liu, Y. Lu, D. Li, Y. Shimodaira, Y. Hosogi, Y. Kuroda and K. Hashimoto, *ACS Nano*, 2012, **6**, 1609–1618.
186 X. Zheng, Z.-P. Shen, C. Cheng, L. Shi, R. Cheng and J. Dong, *RSC Adv.*, 2017, **7**, 52172–52179.
187 Y. Li, C. Zhang, D. Shuai, S. Naraginti, D. Wang and W. Zhang, *Water Res.*, 2016, **106**, 249–258.
188 Q. Li, M. A. Page, B. J. Marinas and J. K. Shang, *Environ. Sci. Technol.*, 2008, **42**, 6148–6153.
189 R. Cheng, L. J. Shen, J. H. Yu, S. Y. Xiang and X. Zheng, *Catalysts*, 2018, **8**, 406.
190 O. Akhavan, M. Choobtashani and E. Ghaderi, *J. Phys. Chem. C*, 2012, **116**, 9653–9659.
191 T. Hasegawa, M. Tamura, K. Satoh, M. Tsujimura, A. Kawamura, C. Thammakarn, H. Hakim, S. Ruenphet and K. Takehara, *J. Vet. Med. Sci.*, 2013, **75**, 1091–1093.
192 K. Takehara, K. Yamazaki, M. Miyazaki, Y. Yamada, S. Ruenphet, A. Jahangir, D. Shoham, M. Okamura and M. Nakamura, *Virus Res.*, 2010, **151**, 102–103.
193 B. L. Carpenter, X. Situ, F. Scholle, J. Bartelmess, W. W. Weare and R. A. Ghiladi, *Molecules*, 2015, **20**, 10604–10621.
194 K. R. Stoll, F. Scholle, J. D. Zhu, X. W. Zhang and R. A. Ghiladi, *Photochem. Photobiol. Sci.*, 2019, **18**, 1923–1932.
195 M. J. Casteel, K. Jayaraj, A. Gold, L. M. Ball and M. D. Sobsey, *Photochem. Photobiol.*, 2010, **80**, 294–300.
196 Y. Si, Z. Zhang, W. Wu, Q. Fu, K. Huang, N. Nitin, B. Ding and G. Sun, *Sci. Adv.*, 2018, **4**, eaar5931.
197 F. Käsermann and C. Kempf, *Antiviral Res.*, 1997, **34**, 65–70.
198 J. Kim, H. Lee, J. Y. Lee, K. H. Park and J. Lee, *Appl. Catal., B*, 2020, **270**, 118862.
199 N. E. Grammatikova, L. George, Z. Ahmed, N. R. Candeias, N. A. Durandin and A. Efimov, *J. Mater. Chem. B*, 2019, **7**, 4379–4384.
200 H. Majiya, O. O. Adeyemi, M. Herod, N. J. Stonehouse and P. Millner, *J. Photochem. Photobiol., B*, 2018, **189**, 87–94.
201 B. K. Mayer, Y. Yang, D. W. Gerrity and M. Abbaszadegan, *Microbiol. Insights*, 2015, **8**, 15–28.
202 T. Tachikawa, M. Fujitsuka and T. Majima, *J. Phys. Chem. C*, 2007, **111**, 5259–5275.
203 A. G. Rincón and C. Pulgarin, *Appl. Catal., B*, 2003, **44**, 263–284.
204 T. Tachikawa and T. Majima, *Langmuir*, 2012, **28**, 8933–8943.
205 L. Mahmoudi, R. Kissner, T. Nauser and W. H. Koppenol, *Biochemistry*, 2016, **55**, 2849–2856.
206 W. Choi, A. Termin and M. R. Hoffmann, *J. Phys. Chem.*, 1994, **98**, 13669–13679.
207 K. Vinodgopal and P. V. Kamat, *Environ. Sci. Technol.*, 1995, **29**, 841–845.
208 J. S. Park and W. Choi, *Langmuir*, 2004, **20**, 11523–11527.
209 N. Wang, Z. Chen, L. Zhu, X. Jiang, B. Lv and H. Tang, *J. Photochem. Photobiol., A*, 2007, **191**, 193–200.
210 S. L. Penrod, T. M. Olson and S. B. Grant, *Langmuir*, 1996, **12**, 5576–5587.
211 K. L. Hardee and A. J. Bard, *J. Electrochem. Soc.*, 1977, **124**, 215–224.
212 T. Tachikawa, S. Tojo, K. Kawai, M. Endo, M. Fujitsuka, T. Ohno, K. Nishijima, Z. Miyamoto and T. Majima, *J. Phys. Chem. B*, 2004, **108**, 19299–19306.
213 S. Livraghi, M. C. Paganini, E. Giamello, A. Selloni, C. Di Valentin and G. Pacchioni, *J. Am. Chem. Soc.*, 2006, **128**, 15666–15671.
214 C. Burda and X. Chen, *J. Am. Chem. Soc.*, 2008, **130**, 5018–5019.
215 H. Irie, S. Miura, K. Kamiya and K. Hashimoto, *Chem. Phys. Lett.*, 2008, **457**, 202–205.
216 R. Asahi, T. Morikawa, T. Ohwaki, K. Aoki and Y. Taga, *Science*, 2001, **293**, 269–271.
217 X. Wang, K. Maeda, A. Thomas, K. Takanabe, G. Xin, J. M. Carlsson, K. Domen and M. Antonietti, *Nat. Mater.*, 2009, **8**, 76–80.

218 A. Kudo and S. Hijii, *Chem. Lett.*, 1999, 1103–1104.
219 J. Yu, G. Dai and B. Huang, *J. Phys. Chem. C*, 2009, **113**, 16394–16401.
220 Z. Yi, J. Ye, N. Kikugawa, T. Kako, S. Ouyang, H. Stuart-Williams, H. Yang, J. Cao, W. Luo and Z. Li, *Nat. Mater.*, 2010, **9**, 559–564.
221 F. Su, S. C. Mathew, G. Lipner, X. Fu, M. Antonietti, S. Blechert and X. Wang, *J. Am. Chem. Soc.*, 2010, **132**, 16299–16301.
222 R. Abe, H. Takami, N. Murakami and B. Ohtani, *J. Am. Chem. Soc.*, 2008, **130**, 7780–7781.
223 J. Kim, C. W. Lee and W. Choi, *Environ. Sci. Technol.*, 2010, **44**, 6849–6854.
224 M. Pineiro, A. L. Carvalho, M. M. Pereira, A. M. D. A. R. Gonsalves, L. G. Arnaut and S. J. Formosinho, *Chem. – Eur. J.*, 1998, **4**, 2299–2307.
225 F. Wilkinson, W. P. Helman and A. B. Ross, *J. Phys. Chem. Ref. Data*, 1993, **22**, 113–262.
226 D. L. Akins, H.-R. Zhu and C. Guo, *J. Phys. Chem.*, 1996, **100**, 5420–5425.
227 H. Ajie, M. M. Alvarez, S. J. Anz, R. D. Beck, F. Diederich, K. Fostiropoulos, D. R. Huffman, W. Kraetschmer and Y. Rubin, *et al.*, *J. Phys. Chem.*, 1990, **94**, 8630–8633.
228 J. W. Arbogast, A. P. Darmanyan, C. S. Foote, F. N. Diederich, R. L. Whetten, Y. Rubin, M. M. Alvarez and S. J. Anz, *J. Phys. Chem.*, 1991, **95**, 11–12.
229 Y. Zeng, L. Biczok and H. Linschitz, *J. Phys. Chem.*, 1992, **96**, 5237–5239.
230 M. Tabata, M. Kumamoto and J. Nishimoto, *Anal. Chem.*, 1996, **68**, 758–762.
231 V. Leen, D. Miscoria, S. Yin, A. Filarowski, J. Molisho Ngongo, M. Van der Auweraer, N. Boens and W. Dehaen, *J. Org. Chem.*, 2011, **76**, 8168–8176.
232 C. Tizaoui, *Ozone: Sci. Eng.*, 2020, **42**, 378–385.
233 G. C. Tremiliosi, L. G. P. Simoes, D. T. Minozzi, R. I. Santos, D. C. B. Vilela, E. L. Durigon, R. R. G. Machado, D. S. Medina, L. K. Ribeiro, I. L. V. Rosa, M. Assis, J. Andrés, E. Longo and L. H. Freitas-Junior, *bioRxiv*, 2020, DOI: 10.1101/2020.06.26.152520.
234 C. Balagna, S. Perero, E. Percivalle, E. V. Nepita and M. Ferraris, *Open Ceram.*, 2020, **1**, 100006.
235 S. S. Jeremiah, K. Miyakawa, T. Morita, Y. Yamaoka and A. Ryo, *Biochem. Biophys. Res. Commun.*, 2020, **533**, 195–200.
236 A. Sen, D. Khona, S. Ghatak, V. Gopalakrishnan, K. Cornetta, S. Roy, S. Khanna and C. Sen, 2020, DOI: 10.26434/chemrxiv.12307214.v1.
237 S. Behzadinasab, A. Chin, M. Hosseini, L. Poon and W. A. Ducker, *ACS Appl. Mater. Interfaces*, 2020, **12**, 34723–34727.
238 M. Hosseini, A. W. Chin, S. Behzadinasab, L. L. Poon and W. A. Ducker, *ACS Appl. Mater. Interfaces*, 2021, **13**, 5919–5928.
239 G. Pezzotti, E. Ohgitani, M. Shin-Ya, T. Adachi, E. Marin, F. Boschetto, W. Zhu and O. Mazda, *bioRxiv*, 2020, DOI: 10.1101/2020.06.19.159970.
240 S. Yuan, H. Chu, K. Zhang, J. Ye, K. Singh, R. Y. Kao, B. K. Chow, J. Zhou and B. J. Zheng, *J. Antimicrob. Chemother.*, 2016, **71**, 2489–2497.
241 L. Decrey, S. Kazama, K. M. Udert and T. Kohn, *Environ. Sci. Technol.*, 2015, **49**, 1060–1067.
242 J. Hasan, A. Pyke, N. Nair, T. Yarlagadda, G. Will, K. Spann and P. K. Yarlagadda, *ACS Biomater. Sci. Eng.*, 2020, **6**, 4858–4861.
243 D. Schoeman and B. C. Fielding, *Virol. J.*, 2019, **16**, 1–22.
244 D. S. Dimitrov, *Nat. Rev. Microbiol.*, 2004, **2**, 109–122.
245 A. Kuzmin, P. Orekhov, R. Astashkin, V. Gordeliy and I. Gushchin, *bioRxiv*, 2021, DOI: 10.1101/2021.03.10.434722.
246 L. Xie, F. Liu, J. Liu and H. Zeng, *ACS Appl. Mater. Interfaces*, 2020, **12**, 58360–58368.
247 L. Javidpour, A. Božič, A. Naji and R. Podgornik, *Soft Matter*, 2021, **17**, 4296–4303.
248 X. Mi, E. K. Bromley, P. U. Joshi, F. Long and C. L. Heldt, *Langmuir*, 2019, **36**, 370–378.
249 A. C. Walls, Y.-J. Park, M. A. Tortorici, A. Wall, A. T. McGuire and D. Veesler, *Cell*, 2020, **181**, 281–292.e286.
250 E. Mantlo, T. Rhodes, J. Boutros, L. Patterson-Fortin, A. Evans and S. Paessler, *F1000Research*, 2020, **9**, 674.
251 N. Hutasoit, B. Kennedy, S. Hamilton, A. Luttick, R. A. Rahman Rashid and S. Palanisamy, *Manuf. Lett.*, 2020, **25**, 93–97.
252 E. Mantlo, S. Paessler, A. V. Seregin and A. T. Mitchell, *Antimicrob. Agents Chemother.*, 2020, **65**, e0139020.
253 C. J. Carlson, A. C. R. Gomez, S. Bansal and S. J. Ryan, *Nat. Commun.*, 2020, **11**, 4312.
254 F. A. Engelbrecht and R. J. Scholes, *One Health*, 2021, **12**, 100202.
255 M. L. Ermini and V. Voliani, *ACS Nano*, 2021, **15**, 6008–6029.
256 A. A. Cortes and J. M. Zuñiga, *Diagn. Microbiol. Infect. Dis.*, 2020, 115176.
257 E. A. Bryce, B. Velapatino, H. Akbari Khorami, T. Donnelly-Pierce, T. Wong, R. Dixon and E. Asselin, *Biointerphases*, 2020, **15**, 011005.
258 B. C. Sousa and D. L. Cote, *MRS Adv.*, 2020, **5**, 2873–2880.
259 S. Chatterjee, J. S. Murallidharan, A. Agrawal and R. Bhardwaj, *Phys. Fluids*, 2021, **33**, 052101.
260 K. Ariga, X. Jia, J. Song, J. P. Hill, D. T. Leong, Y. Jia and J. Li, *Angew. Chem., Int. Ed.*, 2020, **59**, 15424–15446.
261 K. Ariga, *Small Sci.*, 2021, **1**, 2000032.
262 S. Kumar, M. Karmacharya, S. R. Joshi, O. Gulenko, J. Park, G.-H. Kim and Y.-K. Cho, *Nano Lett.*, 2020, **21**, 337–343.
263 S. Kumaran, E. Oh, S. Han and H.-J. Choi, *Nano Lett.*, 2021, **21**, 5422–5429.
264 J. Kobayashi and T. Okano, *Bull. Chem. Soc. Jpn.*, 2019, **92**, 817–824.
265 K. Ariga, X. Jia, J. Song, C. T. Hsieh and S. H. Hsu, *ChemNanoMat*, 2019, **5**, 692–702.
266 J. A. Jackman, A. R. Ferhan and N.-J. Cho, *Bull. Chem. Soc. Jpn.*, 2019, **92**, 1404–1412.
267 H. Huang, R. Jiang, Y. Feng, H. Ouyang, N. Zhou, X. Zhang and Y. Wei, *Nanoscale*, 2020, **12**, 1325–1338.